



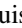

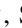
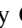





Inferring the Morphology of Stellar Distribution in TNG50: Twisted and Twisted-stretched Shapes

Razieh Emami¹ , Lars Hernquist¹ , Charles Alcock¹, Shy Genel^{2,3} , Sownak Bose¹ , Rainer Weinberger¹ , Mark Vogelsberger⁴ , Xuejian Shen⁵, Joshua S. Speagle^{6,7,8,11} , Federico Marinacci⁹ , John C. Forbes², and Paul Torrey¹⁰ 

¹ Center for Astrophysics, Harvard & Smithsonian, 60 Garden Street, Cambridge, MA 02138, USA; razieh.emami_meibody@cfa.harvard.edu

² Center for Computational Astrophysics, Flatiron Institute, New York, NY, USA

³ Columbia Astrophysics Laboratory, Columbia University, 550 West 120th Street, New York, NY 10027, USA

⁴ Department of Physics, Kavli Institute for Astrophysics and Space Research, Massachusetts Institute of Technology, Cambridge, MA 02139, USA

⁵ TAPIR, California Institute of Technology, Pasadena, CA 91125, USA

⁶ Department of Statistical Sciences, University of Toronto, Toronto, M5S 3G3, Canada

⁷ Dunlap Institute for Astronomy & Astrophysics, University of Toronto, Toronto, M5S 3H4, Canada

⁸ David A. Dunlap Department of Astronomy & Astrophysics, University of Toronto, Toronto, M5S 3H4, Canada

⁹ Department of Physics & Astronomy “Augusto Righi,” University of Bologna, via Gobetti 93/2, I-40129 Bologna, Italy

¹⁰ Department of Astronomy, University of Florida, 211 Bryant Space Sciences Center, Gainesville, FL 32611, USA

Received 2021 January 20; revised 2021 May 26; accepted 2021 June 4; published 2021 August 27

Abstract

We investigate the morphology of the stellar distribution (SD) in a sample of Milky Way–like galaxies in the TNG50 simulation. Using a local in shell iterative method as the main approach, we explicitly show evidence of twisting (in about 52% of halos) and stretching (in 48% of them) in real space. This is matched with the reorientation observed in the eigenvectors of the inertia tensor and gives us a clear picture of having a reoriented SD. We make a comparison between the shape profile of the dark matter (DM) halo and SD and quite remarkably see that their radial profiles are fairly close, especially at small galactocentric radii, where the stellar disk is located. This implies that the DM halo is somewhat aligned with stars in response to the baryonic potential. The level of alignment mostly decreases away from the center. We study the impact of substructures in the orbital circularity parameter. It is demonstrated that in some cases, faraway substructures are counterrotating compared with the central stars and may flip the sign of total angular momentum and thus the orbital circularity parameter. Truncating them above 150 kpc, however, retains the disky structure of the galaxy as per initial selection. Including the impact of substructures in the shape of stars, we explicitly show that their contribution is subdominant. Overlaying our theoretical results on the observational constraints from previous literature, we establish fair agreement.

Unified Astronomy Thesaurus concepts: [Galaxy classification systems \(582\)](#); [Milky Way stellar halo \(1060\)](#); [Hydrodynamical simulations \(767\)](#)

1. Introduction

According to the standard paradigm of galaxy formation, galaxies are formed hierarchically and in multiple phases, where the early formation phase involves the collapse of gas and in situ star formation, while the latter phase includes the accretion and merger of many smaller structures forming the stellar distribution (SD; Searle & Zinn 1978; White & Rees 1978; Blumenthal et al. 1984; White & Frenk 1991; Forbes et al. 1997; Navarro et al. 1997; Oser et al. 2010; Beasley et al. 2018). Such accreted structures lead to the formation of tidal debris in different stages of the phase mixing. Consequently, the SD is expected to retain information regarding the assembly history of the galaxy and can be treated as a direct tracer of the galaxy morphology and evolution.

Observations of the Milky Way (MW) reveal that it has encountered multiple phases of accretion as a buildup of its SD (Ibata et al. 1994; Helmi & White 1999; Helmi et al. 2018; Mackereth & Bovy 2020; Naidu et al. 2020). Such accreted structures complicate observational measurements of the morphology of galaxies. Indeed, there have been many extensive endeavors to measure the shape of the stellar halo (SH) in the MW in real space (Vivas & Zinn 2006; Bell et al. 2008; Ivezić et al. 2008; Watkins et al. 2009; Sesar et al. 2010, 2013;

Deason et al. 2011; Belokurov et al. 2014; Faccioli et al. 2014; Iorio & Belokurov 2019; Kado-Fong et al. 2020) using different stellar types, such as blue horizontal branch (BHB) and blue straggler (BS) stars (Deason et al. 2011), main-sequence turnoff (MSTO) stars (Bell et al. 2008), and RR Lyrae stars (RRLS; Sesar et al. 2013; Iorio & Belokurov 2019), as tracers, or to measure the shape in the velocity space and in terms of the velocity anisotropy (Myeong et al. 2019; Bird et al. 2020; Iorio & Belokurov 2021). However, owing to the aforementioned complexities, as well as the very nontrivial selection functions for the surveys, not all of these observational studies lead to the same final results.

As a result, there have been many attempts to model the galaxy morphology traced by either the dark matter (DM) or SHs), theoretically. In the last decade, there have been many improvements in the study of the morphology of galaxies using hydrodynamical simulations like EAGLE (Crain et al. 2015; Schaye et al. 2015; Trayford et al. 2019; Font et al. 2020), AURIGA (Monachesi et al. 2016; Grand et al. 2018; Hani et al. 2019), NIHAO-UHD (Buck et al. 2018, 2020), and FIRE-2 (El-Badry et al. 2018; Garrison-Kimmel et al. 2018; Orr et al. 2020; Sanderson et al. 2020; Santistevan et al. 2020). Added to the above list, there have also been some investigations using the Illustris simulation (Genel et al. 2014; Vogelsberger et al. 2014a, 2014b; Sijacki et al. 2015) and IllustrisTNG simulations (Marinacci et al. 2018; Naiman et al. 2018; Nelson et al. 2018;

¹¹ Banting Fellow.

Table 1

The Physical Parameters of the TNG50 Simulation, Including the Simulation Volume, Box Side Length, Number of Gas and DM Particles, Baryon and DM Mass, and $z = 0$ Plummer Gravitational Softening for the DM and Stellar Components

Name	Volume ((Mpc) ³)	L_{box} (Mpc h^{-1})	N_{gas}	N_{DM}	m_{baryon} ($10^5 M_{\odot}$)	m_{DM} ($10^5 M_{\odot}$)	$\epsilon_{\text{DM,stars}}$ (kpc h^{-1})
TNG50	51.7 ³	35	2160 ³	2160 ³	0.85	4.5	0.39 \rightarrow 0.195
TNG50-Dark	51.7 ³	35	...	2160 ³	...	5.38	0.39 \rightarrow 0.195

Pillepich et al. 2018; Springel et al. 2018; Merritt et al. 2020; Vogelsberger et al. 2020).

Perhaps the best advantage of using cosmological hydrodynamical simulations is the capability to disentangle the contribution of the central halo and the substructures to the stellar morphology, get rid of the selection biases, and quantify the impact of using different tracers to probe the SH shape. It is very common to use either the DM or SD as different tracers in probing the galaxy morphology.

The latter one, i.e., SD, is also known in the literature as the SH. However, there are some ambiguities between what is theoretically inferred as the SH and its observational selection. While from the theoretical perspective, SH can be defined mostly using the kinematics of stars and the orbital circularity parameter (with a little spatial cut of 5 kpc to eliminate the stars that are members of the MW bulge; Monachesi et al. 2019), observationally, it is defined in a slightly different way, e.g., stars that are not within a couple of kiloparsecs of the disk plane, etc. Although in this paper, we are providing a theoretical study of the stellar morphology, to avoid any confusion for the observers, we wish to use “stellar distribution,” rather than “stellar halo.”

In Emami et al. (2021), we used the TNG50 simulation (Nelson et al. 2019; Pillepich et al. 2019), the highest resolution from the series of IllustrisTNG simulations, and investigated the shape of a sample of MW-like galaxies using the DM as the tracer. We explicitly showed that the DM halo in TNG galaxies is consistent with a triaxial shape and provided evidence for both gradual and abrupt rotations of the DM halo. Since DM gives us an indirect estimate of the galaxy morphology, it is essential to calculate the galaxy morphology using the SD and compare that with the estimated shape from the DM halo. This is rather essential, as measuring the level of rotation in the DM is extremely hard, if not impossible. On the contrary, modeling galaxy morphology using the SD potentially enables us to check how we could measure them using spectroscopic surveys in our Galaxy.

Motivated by this, in the current paper, we analyze the galaxy shape using the SD. We analyze the shape from both the statistical perspective and individual halos. In the latter case, we make some classifications for the shape of the SD, putting them into two main classes: twisted and twisted-stretched galaxies. We report some levels of gradual or rather abrupt rotations for different galaxies in our sample. In addition, we make a comparison between the morphology of the DM halos (Emami et al. 2021) and the current analysis, for which we use the results of our various algorithms. Although the details of such a comparison depend on the method we use, our analysis explicitly shows that in some sense, the DM halo and SD are fairly similar. We study the impact of gravitationally self-bound substructures on the shape of the SD and very remarkably demonstrate that in most cases, their impact is subdominant. Finally, we overlay our theoretical results on top of recent observational measurements and establish a rather fair agreement between the two.

The paper is structured as follows. In Section 2, we review the simulation setup and sample selection. Section 3 presents several different methods to compute the SD shape. Section 4 focuses on analyzing the shape profiles. In Section 5, we explicitly compare the shape of the DM and SH. In Section 6, we study the impact of the substructures in the shape analysis. In Section 7, we make the comparison between our theoretical results and the observational outcome from previous literature. We present a few technical details on the halo classes in Appendix B.

2. Sample of MW-like Galaxies in TNG Simulation

Below, we present a short summary of the TNG50 simulation (Nelson et al. 2019; Pillepich et al. 2019), as well as our sample selections, in a similar way to Emami et al. (2021).

2.1. TNG50 Simulation

The TNG50 is the highest resolution of the IllustrisTNG cosmological hydrodynamical simulations (Nelson et al. 2019; Pillepich et al. 2019). Table 1 describes the parameters of the model and its mass and gravitational force resolution. The simulation contains different components, such as the DM, gas, stars, supermassive black holes (SMBHs), and magnetic fields that are self-consistently evolved with time in a periodic box. More explicitly, starting from $z = 127$ and using the Zel'dovich approximation to generate the initial condition, the system was evolved in time using the AREPO code (Springel 2010) and by solving a set of coupled differential equations for magnetohydrodynamics (MHD) and self-gravity. The latter is treated numerically by using a tree particle mesh algorithm (Springel 2010). In the last column of each row, we present the softening length for DM/stars. It is taken as 0.39 comoving kpc h^{-1} for redshifts above unity and gets lower, down to 0.195 comoving kpc h^{-1} , at lower redshifts.

The cosmological parameters are chosen from Planck Collaboration et al. (2016), with the values $\Omega_b = 0.0486$, $\Omega_m = \Omega_{dm} + \Omega_b = 0.3089$, $\Omega_{\Lambda} = 0.6911$, $h = 0.6774$, $H_0 = 100h$ km s^{-1} Mpc⁻¹, $\sigma_8 = 0.8159$, and $n_s = 0.9667$.

On the other hand, the unresolved astrophysical processes that are used in IllustrisTNG, like star formation, stellar feedback and SMBH formation, growth, and the feedback, are similar to Illustris simulations, with the main differences in (i) the feedback and growth of SMBHs, where in IllustrisTNG, BH-driven winds are produced through an active galactic nucleus feedback model; (ii) the galactic winds, where, unlike the Illustris, the wind particles are isotropic, as they are assigned an initial velocity pointed in a random direction; and (iii) the stellar evolution and gas chemical enrichment, in which the stellar evolution is tracked through three main stellar phases: from the asymptotic giant branch stars (in the mass range 1–8 M_{\odot}), through the core-collapse supernovae, and from the Type Ia supernovae (both in the range 8–100 M_{\odot}). See

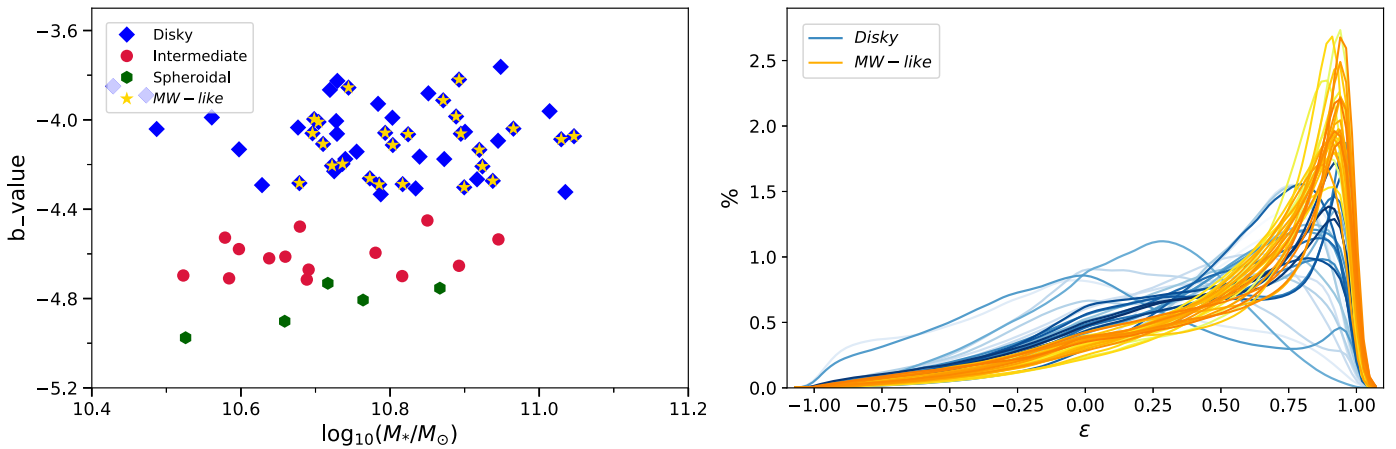


Figure 1. (Left) The b -value vs. the stellar mass for the full sample of galaxies with halo mass in the range $(1-1.6) \times 10^{12} M_\odot$ in TNG50. Yellow stars refer to the distribution of the orbital circularity parameter for the MW-like galaxies in our sample. (Right) Distribution of the orbital circularity parameter, ϵ , for the disk and MW-like halos in our sample. Different halos are shaded using different colors.

Weinberger et al. (2017) and Pillepich et al. (2018) for more details on the IllustrisTNG model.

2.2. MW-like Galaxies in TNG50

As described below, throughout our analysis in this paper, we study a sample of 25 MW-like galaxies with the following common features. On one hand, we propose the DM part of subhalo masses to be restricted in the mass range $(1-1.6) \times 10^{12} M_\odot$, consistent with recent estimates of the MW mass (Posti & Helmi 2019). This brings us a total of 71 galaxies in the above mass range. On the other hand, we require them all to have disklike, rotationally supported morphologies. It was confirmed observationally that the MW shows a manifestly disklike morphology (Schinnerer et al. 2013). Below, we summarize our algorithm, following Abadi et al. (2003) and El-Badry et al. (2018), to identify the disklike galaxies.

2.2.1. Orbital Circularity Parameter

As already mentioned above, throughout our analysis, we are only interested in the rotationally supported MW-like galaxies. The rotational support is measured using the orbital circularity parameter, ϵ , which describes the level of alignment between the angular momentum of the individual stars and the net specific angular momentum of the galaxy,

$$\mathbf{j}_{\text{net}} \equiv \frac{\mathbf{J}_{\text{tot}}}{M} = \frac{\sum_i m_i \mathbf{r}_i \times \mathbf{v}_i}{\sum_i m_i}, \quad (1)$$

where i refers to the star particles, and the sum is performed for all star particles belonging to the simulated galaxy. Pointing the z -axis along with the \mathbf{j}_{net} direction, we compute the inner product of the angular momentum of individual stars and the z -axis, $j_{z,i} = \mathbf{j}_i \cdot \hat{z}$. The orbital circularity parameter is then defined as

$$\epsilon_i \equiv \frac{j_{z,i}}{j_c(E_i)}, \quad j_c(E_i) = r_c v_c = \sqrt{GM(\leq r_c) r_c}, \quad (2)$$

where $j_c(E_i)$ describes the specific angular momentum of the i th stellar particle rotating in a circular orbit, which is specified

with the radius r_c and energy E_i (see Emami et al. 2021 for more details).

Based on our theoretical identification, disk stars are determined to be those with $\epsilon_i \geq 0.7$. Furthermore, we limit our sample to cases where more than 40% of the stars that are in a radial distance less than 10 kpc from the center are disk. This criterion brings us down to a sample of 25 MW-like galaxies.

2.3. Galaxy Classification Based on the b -value

As already mentioned above, in our analysis, we have used the orbital circularity parameter ϵ to determine the MW-like galaxies with a large fraction of stars in the disk. Here we infer the galaxy morphology using a somewhat less used quantity, called the b -value, and compare the final results with the above results; see Emami et al. (2021) for more details. Following the approach of Schulze et al. (2020), the b -value is defined as

$$b = \log_{10} \left(\frac{j_*}{\text{kpc km s}^{-1}} \right) - \frac{2}{3} \log_{10} \left(\frac{M_*}{M_\odot} \right), \quad (3)$$

where j_* refers to the specific angular momentum of stars, while M_* describes the total stellar mass of the galaxy. Based on the above b -value estimate, galaxies can be classified in three main categories as disks (with $b \geq -4.35$), intermediates (with $-4.73 \leq b \leq -4.35$), and spheroidals (with $b < -4.73$). Figure 1 presents the b -value versus the halo stellar mass for the full sample of 71 galaxies in the mass range $(1-1.6) \times 10^{12} M_\odot$, where different galaxy types are marked differently in the figure. Overlaid on the plot, we also show the MW-like galaxies selected from the orbital circularity parameter. Interestingly, all of the inferred as MW-like galaxies are disk, i.e., with $b \geq -4.35$, but not every disk galaxy looks like the MW as inferred from ϵ criteria. Below, we keep our previous galaxy classification and limit our current study to MW-like galaxies. In a future work, we aim to compute the shape of disk galaxies in a broader view and compare them with the sample of MW-like galaxies.

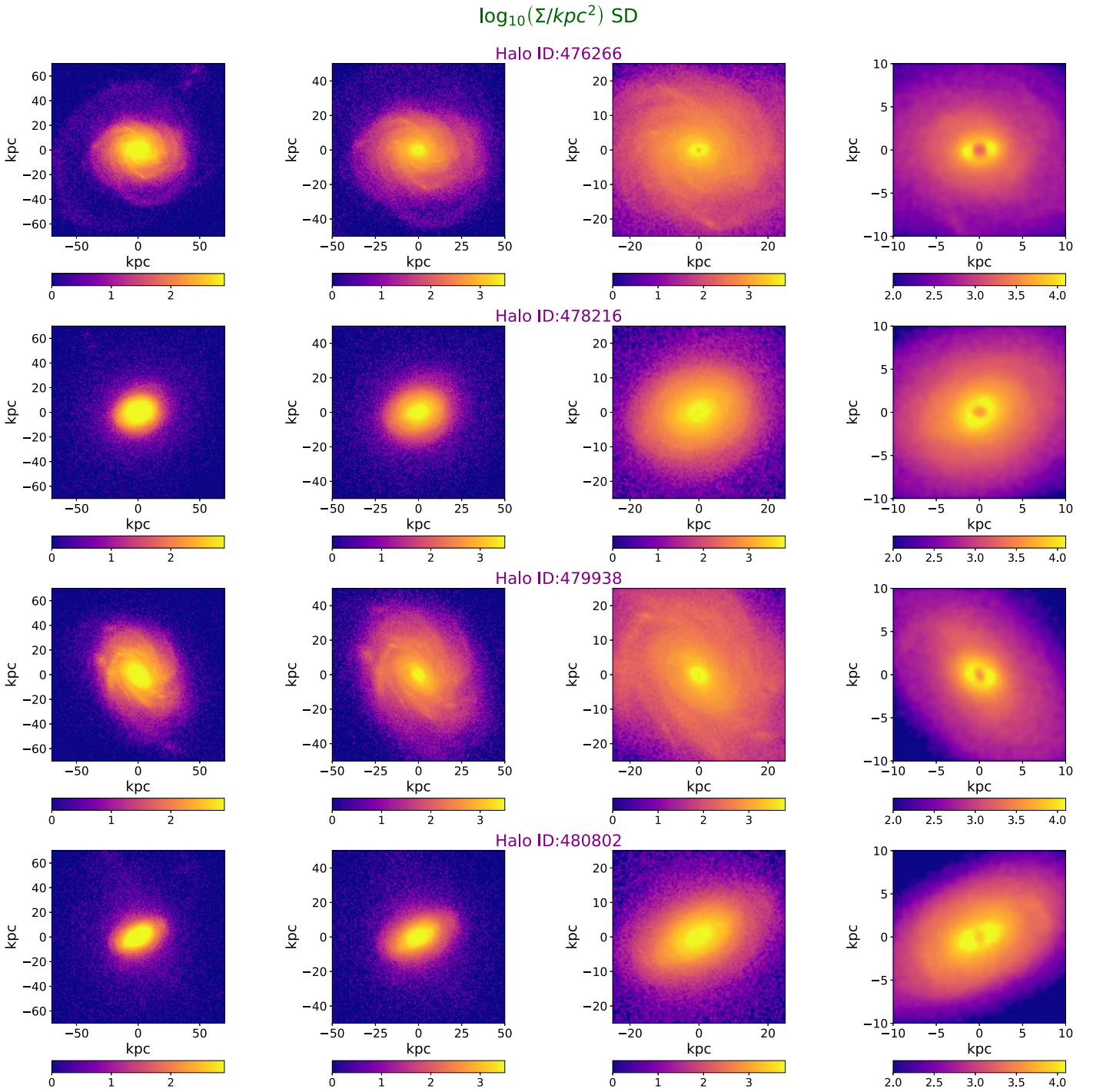


Figure 2. Logarithm of the projected (mass) density map (in units of kpc^{-2}) of SD for a sample of four MW-like galaxies from our galaxy sample in TNG50. Every row presents one galaxy with an ID number. From left to right, we zoom in more on the central part of the halo. We have chosen stars with $|\varepsilon| \leq 1$.

2.4. Mass Density Map

We begin our analysis by presenting the surface number density, Σ , map of SD in a subsample of MW-like galaxies. Figure 2 presents the projected number density map from a subset of four MW-like galaxies in our galaxy sample. In different rows, we refer to various galaxies, while in different columns, we zoom in further down to the central part of the halo. From the figure, it is evident that SD has very complex profiles and substructures. Owing to this, we have to use different algorithms for computing the shape and compare their final outcomes with each other.

3. Main Algorithm in the Shape Analysis

Having introduced a sample of 25 MW-like galaxies, below, we make a comprehensive study of the morphology of the SD as a direct tracer of the galaxy morphology.

Below, we introduce two different algorithms to infer the shape of the SD in depth. We leave the details of the comparison between them to Appendix A.

Depending on the details of the computations, our shape-finder algorithms could be divided into two main classes. In both categories, we infer the shape using iterative methods. In the first approach, we compute the shape using a local shell

iterative method (LSIM), while in the second method, we analyze the SD shape using an enclosed volume iterative method (EVIM). In Emami et al. (2021), we inferred the DM halo shape using EVIM as the primary method. Here, on the other hand, we take LSIM as the main approach. One main reason for this is that star particles are much less abundant than DM particles. This means that the shape is dominated by the few closest shells, and the outer layers contribute much less in the final results. Therefore, EVIM is not able to follow the stellar shapes in much detail locally. This, however, was not a problem for the DM particles, and EVIM was a very useful method to give us the average shape but with many details of what is going on at every radius and in terms of the rotation of the halo.

Having selected LSIM as the main method, we only describe it in what follows and defer the presentation of the EVIM method to Appendix A.

3.1. Local Shell Iterative Method

Here we illustrate the LSIM. In this method, we split the range between the radii $r_{\text{sph}}^i = 2$ and $r_{\text{sph}}^e = 100$ kpc in $N = 100$ logarithmic radial thin shells and compute the reduced inertia tensor as

$$I_{ij} \equiv \left(\frac{1}{M_\star} \right) \times \sum_{n=1}^{N_{\text{part}}} \frac{m_n x_{n,i} x_{n,j}}{R_n^2(r_{\text{sph}})}, \quad i, j = 1, 2, 3, \quad (4)$$

where we have $M_\star \equiv \sum_{n=1}^{N_{\text{part}}} m_n$ and N_{part} describes the total number of star particles inside the thin shell. Furthermore, $x_{n,i}$ refers to the i th coordinate of the n th particle. Finally, $R_n(r_{\text{sph}})$ describes the elliptical radius of the n th particle, defined as

$$R_n^2(r_{\text{sph}}) \equiv \frac{x_n^2}{a^2(r_{\text{sph}})} + \frac{y_n^2}{b^2(r_{\text{sph}})} + \frac{z_n^2}{c^2(r_{\text{sph}})}, \quad (5)$$

where (a, b, c) refer to the axis lengths of the ellipsoid in which we hereafter skip the explicit radius dependence of these functions for brevity. As already mentioned above, in this approach, we compute the shape at some thin shells, where $0.75 \leq R_n^2 \leq 1$. At every radius, we iteratively calculate I_{ij} in the above shells with $a = b = c = r_{\text{sph}}$ in the first iteration. We then use the eigenvalues and eigenvectors of the diagonalized inertia tensor to deform the above shell. In addition, in order to control the deformed ellipsoid, we could take either the interior volume or the semimajor axis fixed. This requires different rescaling of the axis lengths as given by $a = \sqrt{\lambda_1}$, $b = \sqrt{\lambda_2}$, and $c = \sqrt{\lambda_3}$. In the former case, the enclosed volume is kept fixed under the following transformations:

$$\begin{aligned} a &= \frac{r_{\text{sph}}}{(abc)^{1/3}} \sqrt{\lambda_1}, \\ b &= \frac{r_{\text{sph}}}{(abc)^{1/3}} \sqrt{\lambda_2}, \\ c &= \frac{r_{\text{sph}}}{(abc)^{1/3}} \sqrt{\lambda_3}. \end{aligned} \quad (6)$$

Here λ_i , ($i = 1, 2, 3$) describes the eigenvalues of the reduced inertia tensor. In the latter approach, the semimajor axis is

unchanged if

$$\begin{aligned} a &= \frac{r_{\text{sph}}}{\sqrt{\lambda_{\text{max}}}} \sqrt{\lambda_1}, \\ b &= \frac{r_{\text{sph}}}{\sqrt{\lambda_{\text{max}}}} \sqrt{\lambda_2}, \\ c &= \frac{r_{\text{sph}}}{\sqrt{\lambda_{\text{max}}}} \sqrt{\lambda_3}, \end{aligned} \quad (7)$$

where $\lambda_{\text{max}} \equiv \text{Max}[\lambda_i, i = (1, 2, 3)]$.

In what follows, we adopt the former choice, to get as close as possible to the EVIM. We briefly comment on the latter approach as well. Using the eigenvectors of the inertia tensor as the basis, at every iteration, we rotate all of the stars to the frame of the principals, as the coordinate frame defined by the three eigenvectors, and we make sure that they present a right-handed set of coordinates. In order to get statistically reliable results, we require at least 1000 stars in a given shell (Zemp et al. 2011). At all radii, the halo shape is computed as the ratio of the minor to major axis, $s = a/c$, as well as the ratio of the intermediate to major axis, $q = b/c$. We terminate the iteration process once the residual of the shape parameters, (s, q) , after each iteration gets converged to some level defined by $\text{Max} [((s - s_{\text{old}})/s)^2, ((q - q_{\text{old}})/q)^2] \leq 10^{-3}$, with Max referring to the maximum value between the above two quantities. In the following, we only present the points for which the above algorithm has converged.

4. Shape Profile Analysis

Having presented different algorithms for analyzing the shape of the SD, below, we analyze the shape at two different levels: from a statistical and an individual perspective.

4.1. Shape Analysis: Ensemble-based Approach

Starting from the ensemble approach, in Figure 3, we present the radial profile of the median and 16th (84th) percentiles for shape parameters (s, q, T) in both the LSIM and EVIM, where $T \equiv \frac{1 - (b/c)^2}{1 - (a/c)^2}$ refers to the triaxiality parameter. From the figure, it is evident that both versions of LSIM lead to similar radial profiles for the shape parameters. On the other hand, EVIM gives us a flatter radial curve, especially toward the outskirts of the halo. In addition, while the results of the EVIM for (q, T) are in close proximity to the ones from LSIM, it predicts smaller values for the radial profile of the s parameter compared with the LSIM. This is understood, as in the LSIM, less populated outer shells have a larger s parameter, since the halo is getting rounder in the outskirts. On the contrary, the EVIM cannot capture such a variation, as the higher density of stars part of the inner part of the galaxy predominate the results of the shape analysis compared with the outer stars. On the other hand, since the q parameter has a more constant profile with less variation, both techniques give similar results.

Another interesting aspect of Figure 3 is that the median and percentiles of the triaxiality parameter point to an oblate/triaxial SD. In more detail, the inferred T profile from both versions of LSIM is oblate in the central part of galaxy and becomes triaxial in the outskirts. This is in contrast to the T profile from the EVIM, which is more triaxial in the central part of the galaxy and gets converted to an oblate shape at the outskirts.

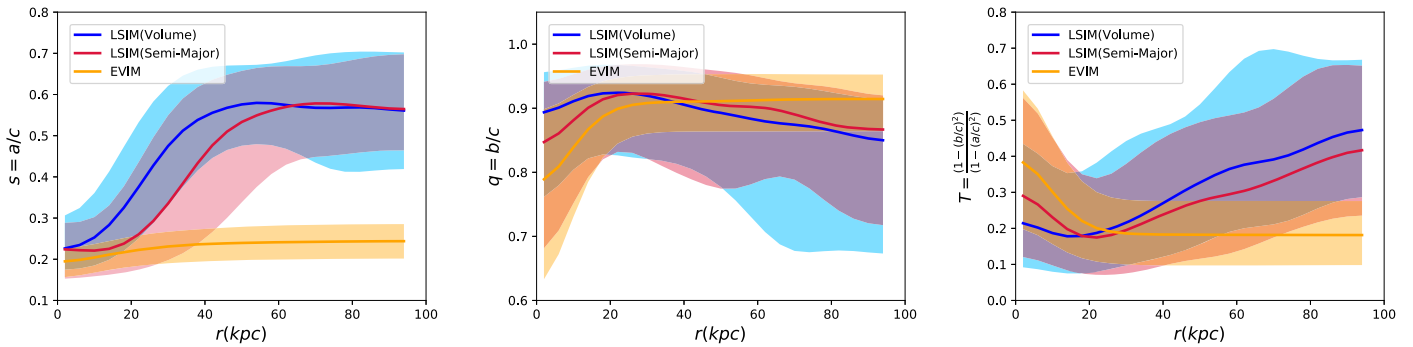


Figure 3. Median and 16th (84th) percentiles of shape parameters (s , q , T) using three different algorithms. We studied the shape using two different versions of LSIM and EVIM. In LSIM(Volume), we compute the shape in local shells with an enclosed volume fixed, while in LSIM(Semi-Major), we keep the semimajor axis fixed.

Table 2

Median and 16th (84th) Percentiles of SD Shape Parameters Computed from LSIM(Volume), LSIM(Semi-Major), and EVIM

Method	s	q	T
LSIM(Volume)	$0.31^{+0.188}_{-0.103}$	$0.93^{+0.039}_{-0.084}$	$0.19^{+0.215}_{-0.113}$
LSIM(Semi-Major)	$0.24^{+0.109}_{-0.070}$	$0.92^{+0.046}_{-0.102}$	$0.18^{+0.214}_{-0.105}$
EVIM	$0.22^{+0.036}_{-0.038}$	$0.90^{+0.046}_{-0.050}$	$0.19^{+0.092}_{-0.089}$

Note. These values are computed in the range $2 \leq r/\text{kpc} \leq 40$.

Table 2 presents the median and 16th (84th) percentiles of the shape parameters (s , q , T) for the above three algorithms where the median/percentiles have been computed in the range $2 \leq r/\text{kpc} \leq 40$. It is worth pointing out that the median/percentiles depend on the upper cutoff of the radius. We have chosen the above cutoff such that most of the galaxies have enough converged points in the shape analysis (see the individual shape analysis for more detail). Being mindful of the dependency of the above values on the upper limit of the radius, it is interesting that statistically (up to 40 kpc), the s from the LSIM with a fixed semimajor axis is closer to the EVIM. However, q is closer between both versions of the LSIM than in the EVIM.

The above ensemble-based analysis gives us a good sense of the collective behavior of the MW-like galaxies in our sample. However, to get a more detailed sense of the morphology of different SDs, in the following, we turn our attention to the shape analysis at the level of individual galaxies.

4.2. Shape Analysis: Individual Galaxy Approach

Having presented the SD shape at the statistical level, below, we analyze the shape for individual galaxies. The main goal is to make a classification of different SD types based on the shape of the SD. As already mentioned above, we use LSIM (Volume) as the main algorithm. However, to make a fair comparison between the above three algorithms, we present the radial profile of the shape parameters for a few galaxies using all of these methods and compare them in depth. We then make a galaxy classification using LSIM(Volume).

Figure 4 compares the radial profile of the shape parameters inferred from the above algorithms. From the figure, it is evident that the results of LSIM(Volume) and LSIM(Semi-Major) are very similar. The inferred shape parameters from EVIM, on the contrary, are very smooth and rarely change after a radius of about 20 kpc. This indicates that in EVIM, the shape

of the outer layers is mostly biased by the interior layers and is a direct consequence of the fact that the stellar density drops sharply toward the outer part of the galaxies. Owing to this, we hereafter skip presenting the results from EVIM. In addition, as the results from different versions of LSIM are fairly close, we just present the results from LSIM(Volume) as the main method. Having compared the outcome of different shape-finder algorithms, below, we focus on the SD shape from individual galaxies and use this to classify SDs in our galaxy sample.

Following the approach of Emami et al. (2021), we put SDs into two main classes: (i) twisted and (ii) twisted-stretched galaxies. It is shown in Appendix B that galaxies belonging to the aforementioned categories behave differently in terms of the radial profile of their eigenvectors. More specifically, while the twisted galaxies present a rather gradual rotation, twisted-stretched galaxies may experience both a gradual and an abrupt rotation radially.

Below, we describe each of these classes in some depth, and we present one example from each class. More details about the entire galaxy sample are found in Appendix B.

4.2.1. Twisted Galaxies

Galaxies belonging to this category show some level of gradual rotation in their radial profiles. To quantify the twists, we shall compute the angles between the sorted eigenvectors (min, inter, max) with different fixed vectors in 3D, such as $L_{\text{tot}}^{\parallel}$, which refers to the total angular momentum of stars, and three bases of the Cartesian coordinate system in the TNG box, i.e., \hat{i} , \hat{j} , and \hat{k} . The amount of total rotation differs from one halo to another. There are 13 galaxies in this category. The radial profiles of such galaxies are presented in Appendix B.

In the analysis of the angle of different eigenvectors with the TNG basis and total angular momentum, we have mapped the angles from $[0, 2\pi]$ to the one from $[0, \pi]$, mainly because $\cos \theta$ is complete in this interval and $\arccos \theta$ is taken in this half-plane. Such selection may lead to some bounces when the angles get to their boundaries, either below zero or above 180° . For example, in galaxy 6, with ID number 488530, the angle between the maximum eigenvector and \hat{i} approaches zero at 3 kpc and bounces off. It is not completely clear whether the angle would go below zero or if this is truly bouncing off. Nevertheless, such behavior would not change the galaxy classification for this because this galaxy has already experienced enough of the gradual rotation to be identified as a twisted galaxy.

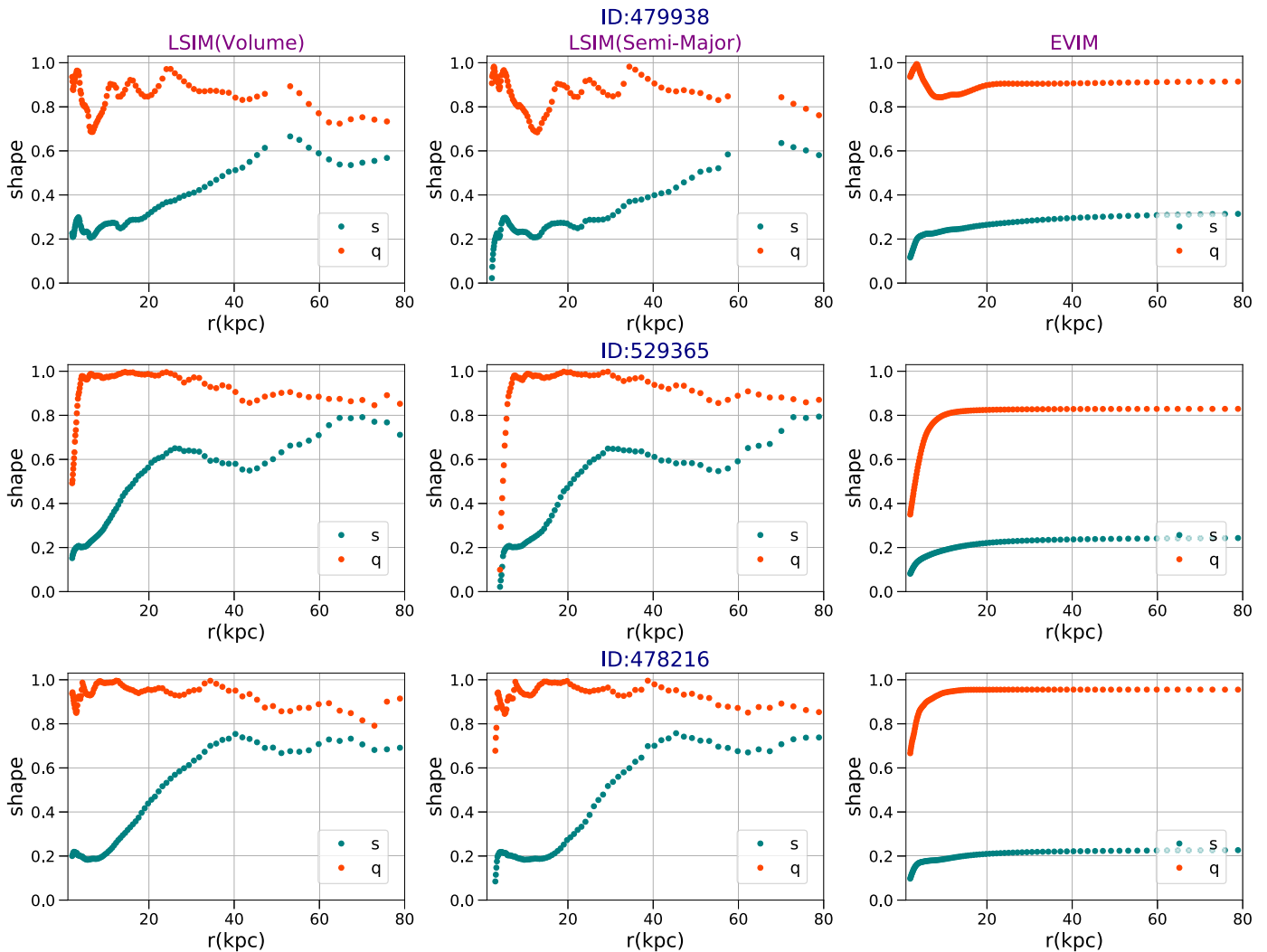


Figure 4. Comparison between the radial profile of the shape parameters using three different algorithms: LSIM(Volume), LSIM(Semi-Major), and EVIM.

4.2.2. Twisted-stretched Galaxies

As the second class, here we describe the twisted-stretched galaxies. In brief, such galaxies may demonstrate both gradual (owing to the galaxy twist) and abrupt (because of the galaxy stretching) rotations in their radial profiles. Galaxies in this class may also be cases for which it is rather hard to distinguish whether the large rotation is due to the twist, the stretching, or both simultaneously. Here stretching occurs when the ordering between different eigenvalues changes at some radii. Consequently, the angles of the corresponding eigenvectors with different fixed vectors are expected to change by 90° owing to the orthogonality of the different eigenvectors. However, since the galaxy itself is also rotating, in some galaxies, these two rotations get mixed, and it is difficult to fully distinguish them. Galaxy 23, with ID number 530330, is one such galaxy. In this galaxy, around the crossing radii at a radius of 10 kpc, the angles of the associated eigenvectors to the intermediate and maximum eigenvalues do not change by 90° . It might well be that the galaxy is also rotating in the opposite direction and thus the net rotation is less than 90° , but it is hard to confirm this. Owing to this, we classify galaxy 23 as twisted-stretched. There are a total of 12 galaxies in this class. Having introduced different classes of galaxies, in Figure 5, we present one example for each of the above classes.

The first example refers to a twisted galaxy in which the galaxy experiences a gradual rotation from the inner to the outer part of the galaxy. The second example, on the other hand, describes a twisted-stretched galaxy with a more abrupt change of axis.

4.3. Impact of the Threshold ϵ on the Shape Analysis

So far, we have computed the SD shape using “all” of the stars out to 100 kpc. In the interest of connecting the SD to what is commonly referred to as the SH (from theoretical grounds), defined in terms of a cut in the orbital circularity parameter, below, we briefly examine the impact of choosing stars with different ϵ thresholds in the shape of the SD. We restrict our current study to the impact of ϵ on the shape parameters and skip considering its effect on the directionality of the eigenvectors. Monachesi et al. (2019) defined the SH based on stars with $\epsilon \leq 0.7$. Here we explore the impact of changing the cutoff in ϵ in the range $\epsilon \in [0.6, 0.7, 0.8, 1.0]$ in the stellar morphology. More explicitly, each time, we mask out all stars that have ϵ above the aforementioned thresholds and compute the shape accordingly.

Figure 6 presents the radial profile of the median and 16th (84th) percentiles of the shape parameters, (s , q , T), for the above thresholds.

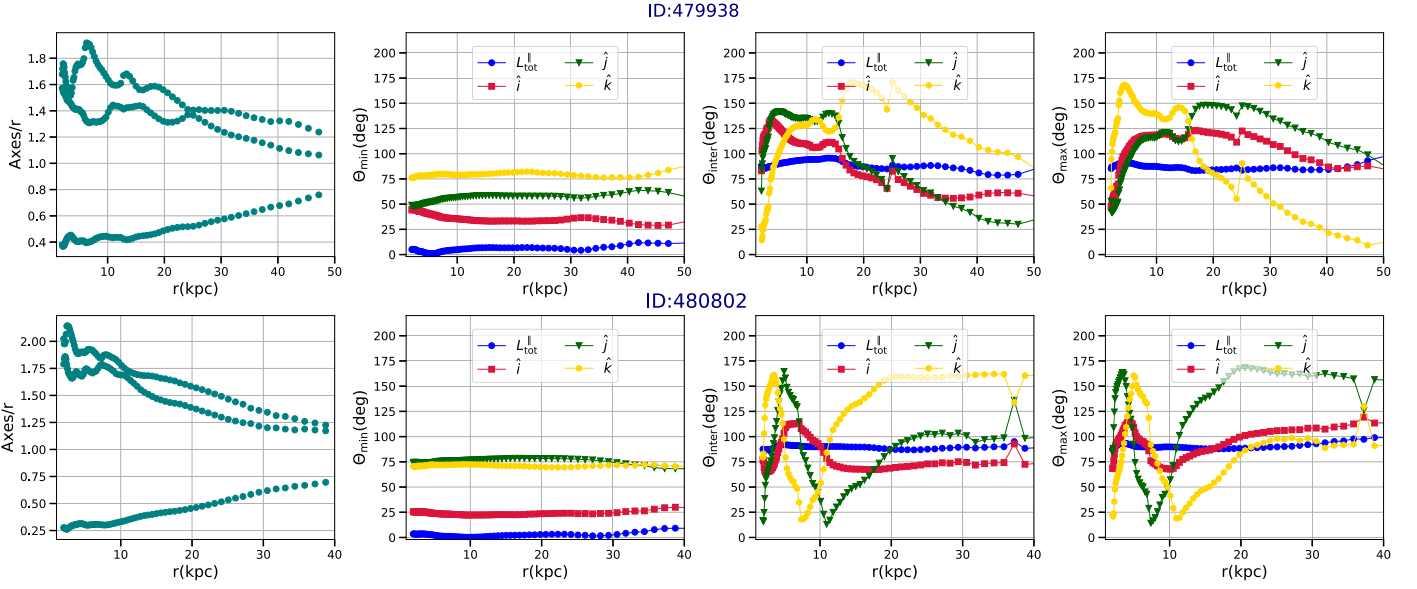


Figure 5. Radial profile of the Axes/r , as well as the angle of min-inter-max eigenvectors with few fixed vectors in space. Top panels: example of a twisted galaxy. Bottom panels: example of a twisted-stretched galaxy.

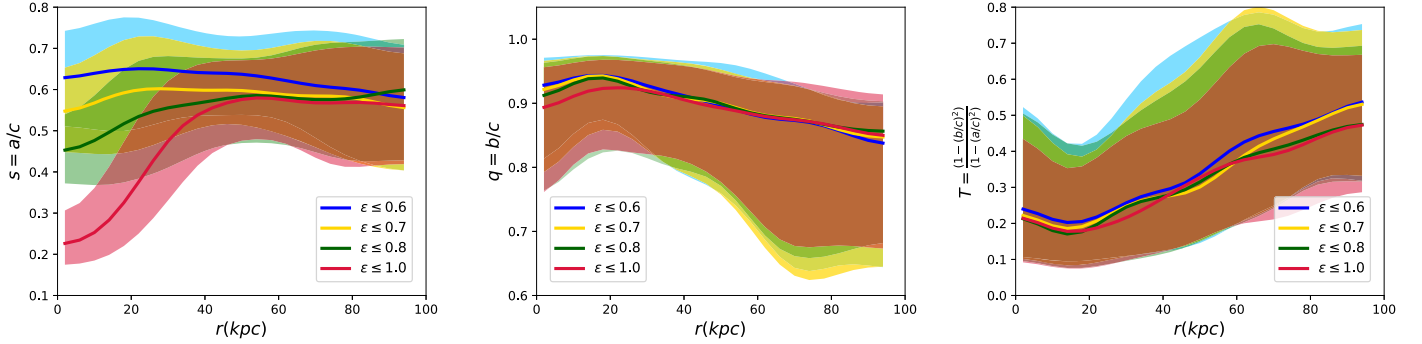


Figure 6. Impact of changing the threshold of ε on the radial profile of the median and 16th (84th) percentiles of the shape parameters.

Quite interestingly, increasing the upper limit in ε decreases the profile of the median (percentiles) of s at smaller radii, where disk stars are mostly located. This is to be expected, as by increasing the threshold of ε , we add more rotationally supported stars, which are part of the stellar disk. Subsequently, the shape becomes progressively more oblate. Owing to this, different lines with various ε do not converge at very small radii. On the contrary, this does not significantly affect the radial profile of the median (percentiles) of q . Consequently, the radial profile of the percentiles of T only slightly shifts down.

Table 3 summarizes the median and percentiles of the shape parameters for the above thresholds. In our analysis, we limit the radial range to $2 \leq r/\text{kpc} \leq 40$. From the table, it is inferred that increasing the threshold in ε decreases the median of all of the shape parameters. However, the amount of suppression in s is larger than the changes in q . This is understood, as increasing the threshold in ε makes the galaxy more oblate and thus further decreases the median of s .

4.4. Different Visualizations of the SD

Having presented the shape profile for individual galaxies, here we make different visualizations for typical galaxies in the above two classes of SDs.

Table 3
Median and 16th (84th) Percentiles of SD Shape Parameters as a Function of the Threshold in ε

Threshold	s	q	T
$\varepsilon \leq 0.6$	$0.641^{+0.118}_{-0.132}$	$0.942^{+0.034}_{-0.059}$	$0.204^{+0.181}_{-0.115}$
$\varepsilon \leq 0.7$	$0.595^{+0.126}_{-0.146}$	$0.941^{+0.033}_{-0.074}$	$0.195^{+0.173}_{-0.112}$
$\varepsilon \leq 0.8$	$0.537^{+0.121}_{-0.153}$	$0.934^{+0.037}_{-0.122}$	$0.191^{+0.206}_{-0.110}$
$\varepsilon \leq 1.0$	$0.308^{+0.188}_{-0.103}$	$0.926^{+0.039}_{-0.084}$	$0.189^{+0.215}_{-0.113}$

Note. These values are computed in the range $2 \leq r/\text{kpc} \leq 40$.

In Figures 7 and 8, we present the 2D projected surface density for one example of the twisted and twisted-stretched galaxies, respectively. In each figure, we present the surface density at a few different radii. In each radius, we use the results of the shape analysis after the convergence and make an image using the stars corresponding to this radius. From the figures, it is evident that the galaxy is rotating in Figure 7, while it is stretching in Figure 8.

Moving to 3D, in Figures 9 and 10, we present the trajectory of the 3D eigenvectors of the inertia tensor for the same twisted and twisted-stretched galaxies as above. Evidently, while the twisted galaxy shows a rather gradual rotation in a wider range of locations, the twisted-stretched galaxy experiences a more

Twisted, ID:501725

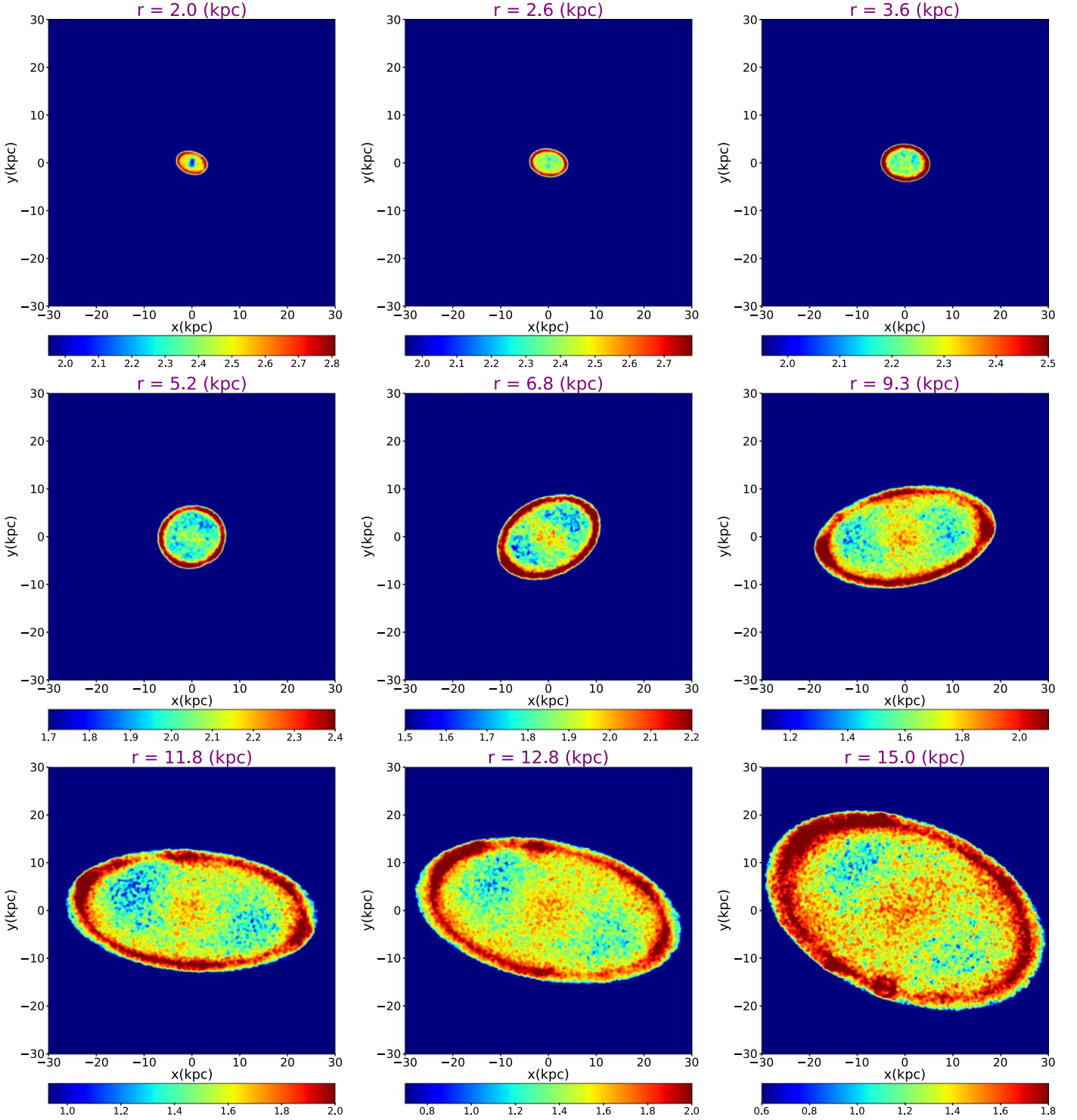


Figure 7. A 2D projection of the surface density of the mass in 3D thin shells (in units of $10^5 \times M_{\odot} \text{ kpc}^{-2}$) for a twisted SD. Evidently, the galaxy is reorienting at different radii. We have computed the projection along a fixed direction in space, the z -direction in the TNG coordinate.

abrupt change of angles in its radial profiles. That is to say that maybe the most visible difference between these galaxies comes back to the abruptness of the transition of angles. Finally, it is crucial to note that if the axis ratio of the axes that are reorienting is not close to unity, then we are certainly not dealing with a stretching but a twisting.

5. Comparison between the Shape of the DM and the SD

Having computed the shape of the SD in detail, here we make some comparisons between the eigenvectors of the inertia tensor associated with the DM halo, inferred from Emami et al. (2021), and the results of this work for the SD. In Emami et al. (2021), we used the EVIM as the main algorithm, while here

Twisted-Stretched, ID:506720

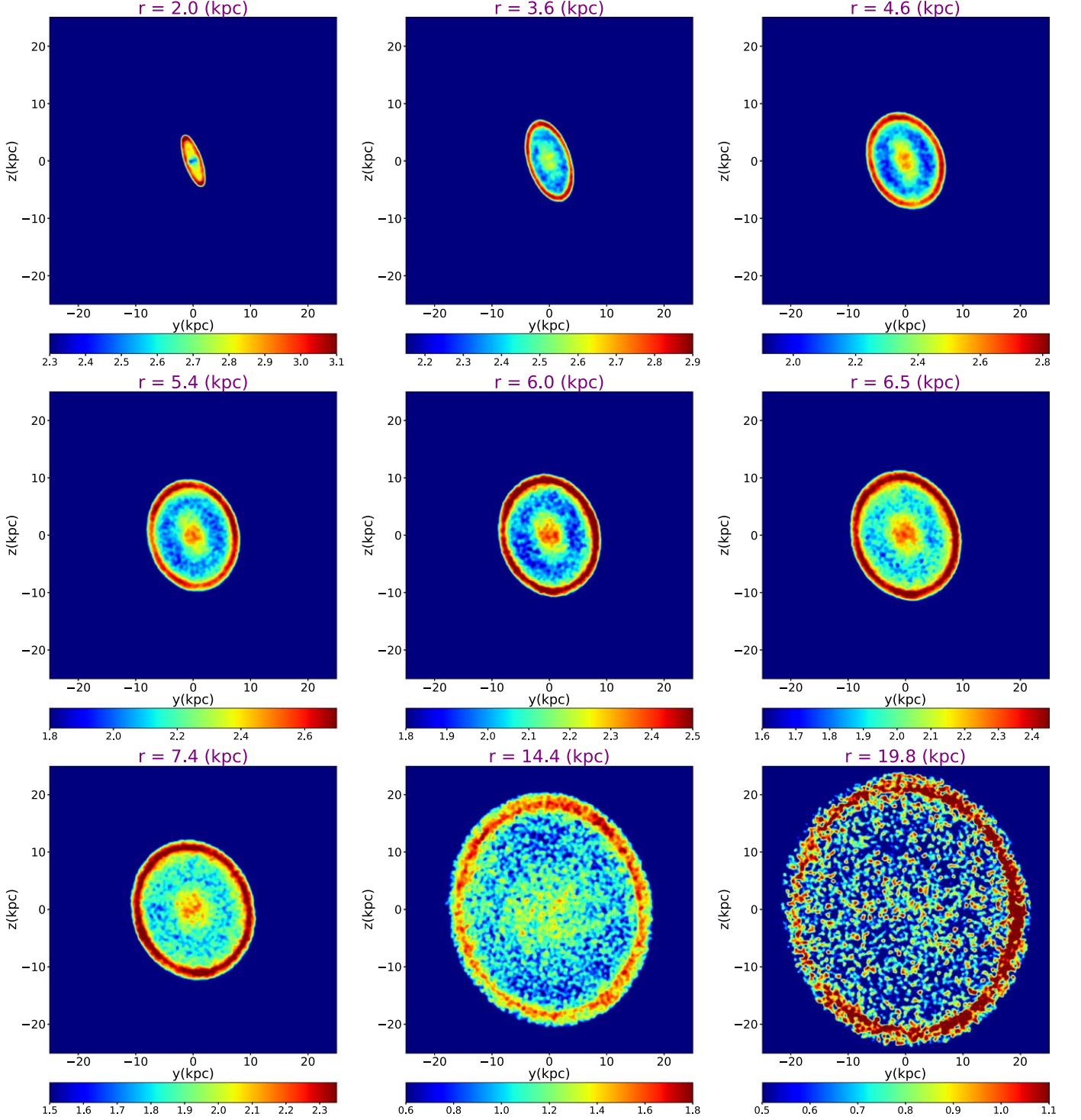


Figure 8. A 2D projection of the surface density (in units of $10^5 \times M_{\odot} \text{ kpc}^{-2}$) for a twisted-stretched SD. Starting from an oblate shape in 3D initially, the galaxy is stretching and becoming more spherical at larger radii. We have computed the projection along the x -direction in the TNG coordinate.

we mainly use the LSIM. Therefore, we do the comparison separately using both of these approaches. As we point out in what follows, this enables us to look at the correlations in both the enclosed sense, from the EVIM, and locally, from the LSIM. Our expectation is that the EVIM method gives us smoother profiles, while the LSIM provides more radially varying correlations. To make the comparison, we take the following steps.

- (i) Make the same radial bins for both DM and SD and compute the shape for each using both EVIM and LSIM separately.
- (ii) Mask over the radii and only look at the radii in which both of these algorithms have converged.
- (iii) Compute the angles between V_{DM} and V_{SD} , which refer to the eigenvectors of the DM and SD, respectively. Since we have three sets of orthogonal vectors, we end up

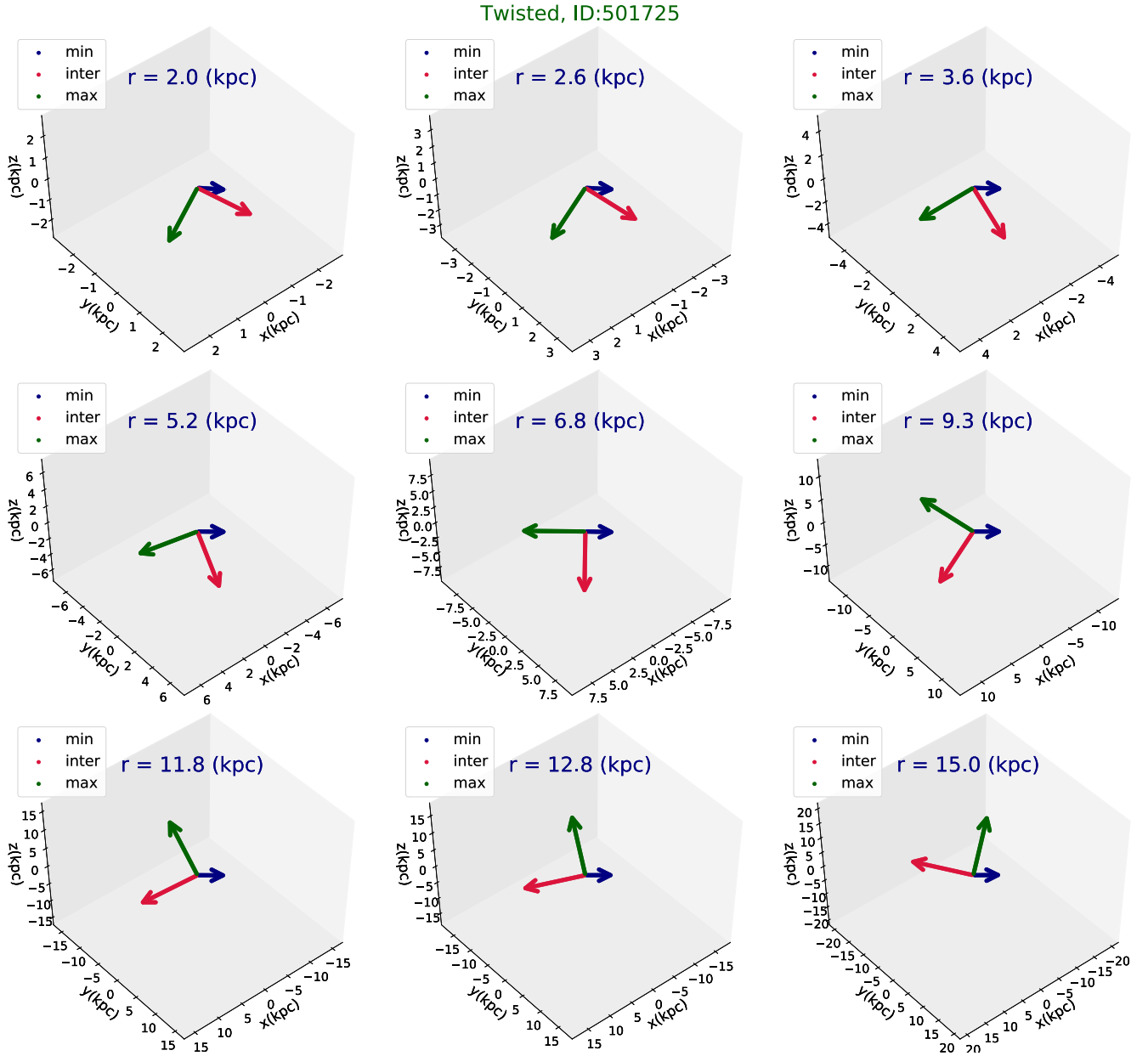


Figure 9. A 3D orientation of the reduced inertia tensor for a twisted galaxy. There is a smooth rotation in the orientation of different eigenvectors radially.

having nine different angles. Sorting the eigenvectors in terms of min, inter, and max eigenvalues, we get the following array of angles at every location:

$$\Theta = [\theta_{\text{mi-mi}}, \theta_{\text{mi-in}}, \theta_{\text{mi-ma}}, \theta_{\text{in-mi}}, \theta_{\text{in-in}}, \theta_{\text{in-ma}}, \theta_{\text{ma-mi}}, \theta_{\text{ma-in}}, \theta_{\text{ma-ma}}], \quad (8)$$

where we have used (mi, in, ma) to replace (min, inter, max) for the sake of brevity. In addition, the first index refers to DM, while the second one describes the SD.

As we have sorted the eigenvectors according to their corresponding eigenvalues, a good test for the similarity of the DM and SD would be to check the magnitude of the mi–mi, in–in, and ma–ma angles. The smaller these values are, the more similar the orientation of the DM halo and SD would be. Owing to this, in what follows, we place special emphasis on the magnitude of these angles. In Figures 11 and 12, we present all nine of the above angles from the EVIM and LSIM,

respectively. To make the above three angles more manifest, we have plotted them with slightly thicker lines and the following color sets: mi–mi (dashed red), in–in (solid orange), and ma–ma (dashed blue). Below, we describe a few common features of these comparisons.

(1) First and foremost, comparing Figure 11 with Figure 12, it is evident that while the mi–mi angle is fairly small and stable, the radial profiles of in–in and ma–ma are a lot more fluctuating in LSIM than in EVIM. That makes sense, as in LSIM, the intermediate and maximum eigenvalues are swinging a lot, and sometimes it is very hard to distinguish them from each other. However, since their corresponding eigenvectors are orthogonal to each other, wherever these lines swing around each other, the angle profile gets dominated by noise. So care must be taken when we compare these profiles with LSIM.

(2) The fact that mi–mi is fairly small in both of these methods is very intriguing, demonstrating that the symmetric

Twisted-Stretched, ID:506720

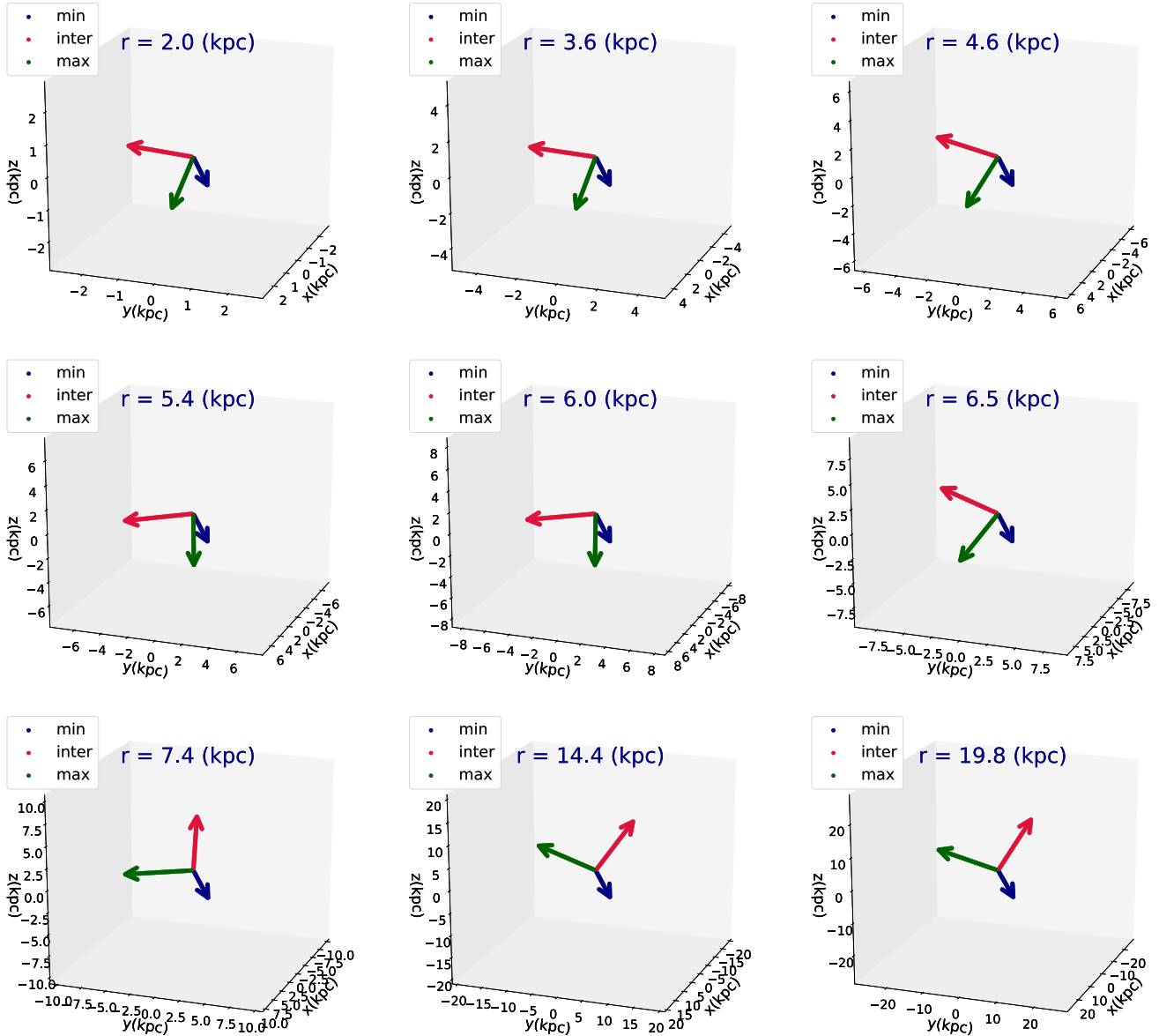


Figure 10. A 3D orientation of the reduced inertia tensor for a twisted-stretched galaxy. There is a quick rotation in the orientation of different eigenvectors radially.

axes of DM and SD are fairly matched. This is because the min eigenvectors in both cases are pointing toward the total angular momentum of the system. This observation confirms that in most cases, the symmetry axes of DM and SD are almost aligned with each other. At smaller radii, this seems to be very natural and might be due to the interaction of the DM halo with the stellar disk. Owing to this interaction, the DM halo is getting aligned with the total angular momentum of the stars. In some cases, such alignment remains the same at larger radii. Others show some levels of misalignment farther out from the center, though. For instance, galaxies 3, 8, and 9 are such cases.

The alignment between m_i – m_i which are mostly aligned with the angular momentum of the disk stars is in great agreement with the results from the previous literature.

Bailin et al. (2005) explored the alignment of the DM halo and the stellar disk in a suite of seven cosmological hydrodynamical simulations. They found that the inner part of the halo,

$r < 0.1R_{\text{vir}}$, is aligned with the disk such that the DM minor axis is well aligned with the stellar disk axis. In contrast, the outer part of the halo, $r > 0.1R_{\text{vir}}$, is unaffected by the stellar disk.

Tenneti et al. (2014) analyzed the shape and alignment of the DM halo and stars for a wide range of subhalo masses, 10^{10} – $6 \times 10^{14} M_{\odot}/h$, in the MassiveBlack-II simulation. They reported a fair level of alignment between the aforementioned components, with a mean misalignment angle decreasing in the range 10° – 30° when increasing the mass in the above range.

Shao et al. (2016) studied the alignment in a sample of the central galaxies and the DM halo from the EAGLE simulation and reported some levels of alignment between them, especially in the inner part of the halo (within 10 kpc from the center). They reported a median misalignment angle of about 33° between the central galaxy and the DM halo.

Prada et al. (2019) studied the radial profile of the alignment between the DM halo and the stellar disk in a sample of 30

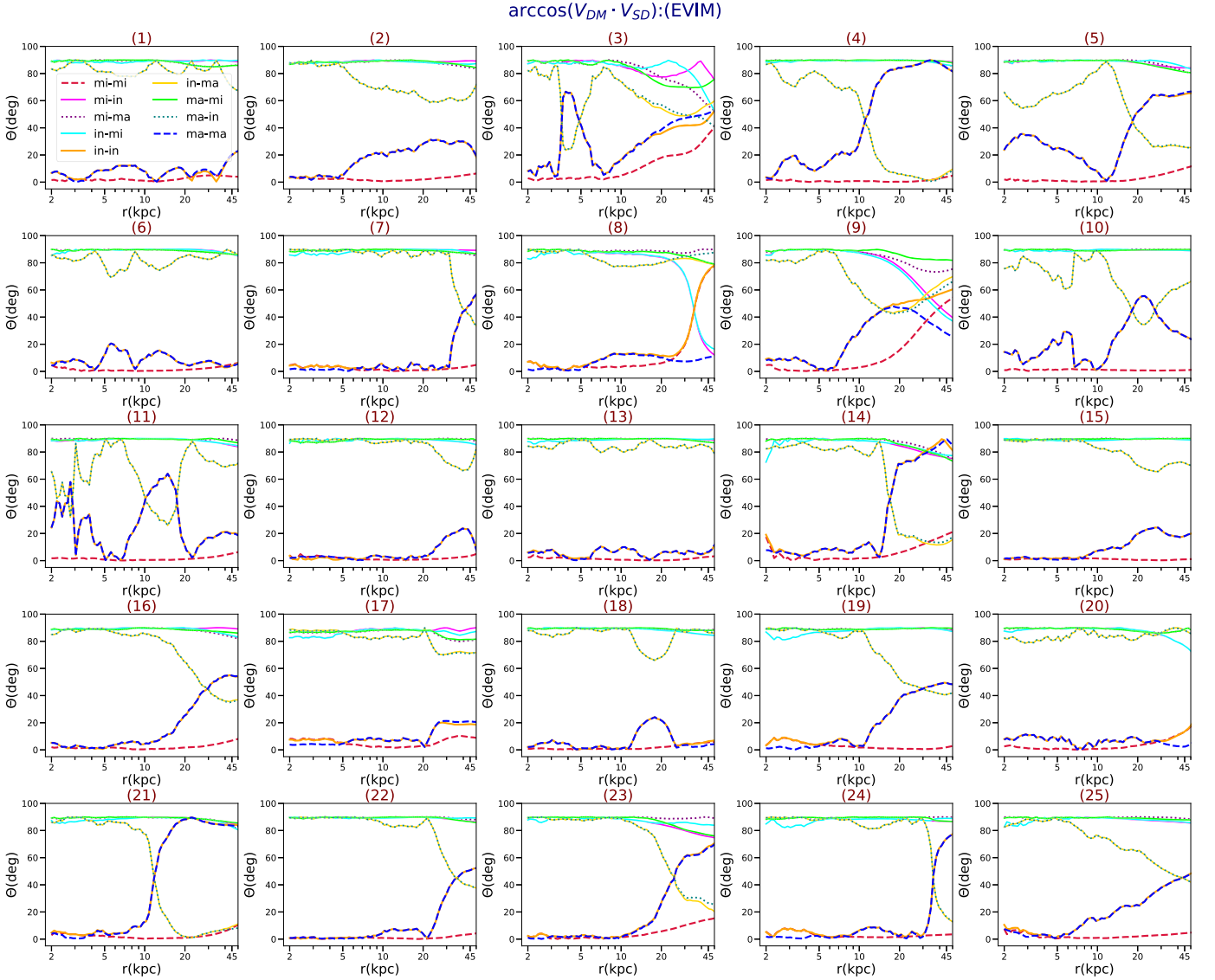


Figure 11. Comparison between the radial profile of the angles of different eigenvectors of the DM halo and SD using the EVIM. The eigenvectors are ordered as (min, inter, max), which are shown as (mi, in, ma) for brevity. There are a total of nine different angles. The DM halo and SD are more similar if the min–min, inter–inter, and max–max angles are minimal and the rest of them are maximal.

MW-like galaxies from the Auriga simulation and found a very high level of alignment between these vectors in most galaxies in their sample and at various radii. Additionally, they reported a significant change in the alignment in some cases, implying some level of twists.

(3) From Figure 11, it is evident that in most cases, the radial profiles of in–in and ma–ma are fairly small close to the center. However, in more than half of galaxies, the angle starts enhancing farther out from the center and gets to its maximum value at larger radii. This means that beyond the typical size of the disk, about 10 kpc, DM and SH profiles are getting misaligned in the plane perpendicular to the total angular momentum. Although very oscillatory, the same conclusion may be drawn for Figure 12 as well. The main reason for this is that any time the inter and max eigenvalues cross each other, the curve of in–in and ma–ma gets enhanced, and the other two angles, in–ma and ma–in, decrease. This indicates that it could be very challenging to identify the inter and max eigenvectors that are matched from DM to SD when the swing occurs. Being

mindful of this technical difficulty, it is fair to say that by a broad majority, the radial profile of the eigenvectors of DM and SD in the stellar disk plane are rather close. They may, however, get misaligned beyond the disk scale.

(4) In summary, it seems that the profiles of the DM and SD are fairly similar within the stellar disk. In the plane of the disk, their eigenvectors get misaligned, while they remain mostly aligned perpendicular to the stellar disk.

Finally, to get a 3D intuition regarding to the similarity of the DM and SD profiles, in Figure 13, we present the 3D trajectory of the eigenvectors of a twisted galaxy at a few different locations. Solid lines describe the DM profile, while dashed lines refer to the SH. It is evidently seen that both the EVIM and LSIM predict similar profiles for the eigenvectors of the DM and SH. Consequently, the min, inter, and max eigenvectors from these two approaches are fairly close. However, this does not entirely hold, and at the last radii, the galaxy experiences another rotation in which the inter and max eigenvectors become perpendicular to each other.

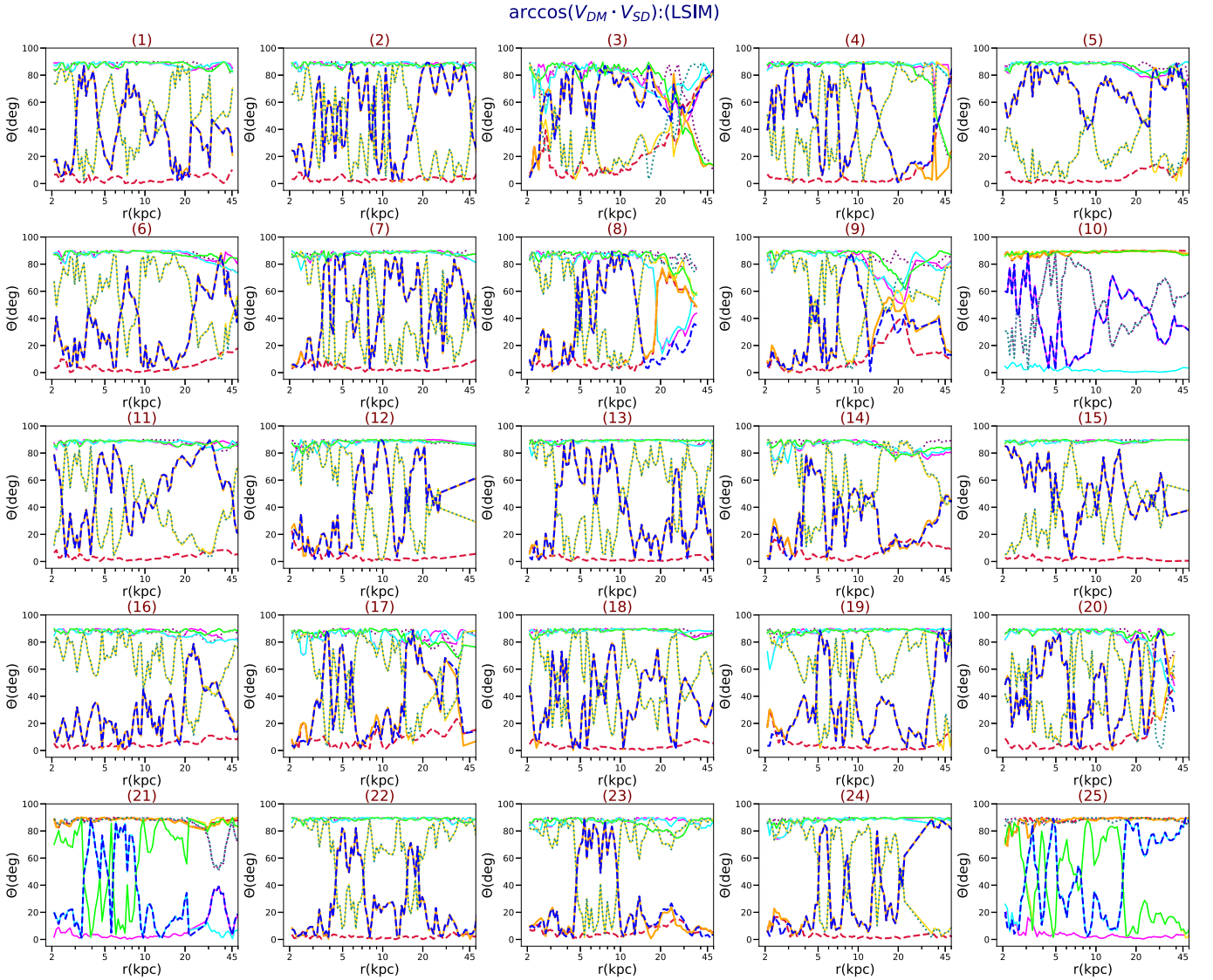


Figure 12. Comparison between the radial profile of the angles of different eigenvectors of the DM halo and SD using the LSIM. See the caption of Figure 11 for more details.

6. Connection to Substructure

So far, we have only investigated the impact of central galaxies in our analysis. Below, we generalize our consideration and analyze the impact of different substructures by using the Friend of Friend (FoF) group catalog in galaxy morphologies. We particularly study the impact of substructures on the orbital circularity parameter and the shape of the SH.

6.1. Impact of FoF Substructures on ε

Here we study the impact of substructures in the orbital circularity parameter, ε . As it turns out, the positions of substructures are essential in determining the radial distribution of ε . Stellar particles located very far away from the galactic center may have a dominant impact on the total angular momentum of the SD while having no effect on the angular momentum of the disk. Subsequently, depending on their orbital motions, in some cases, they may counterrotate with respect to the disk particles, located at $r \leq 10$ kpc, and thus shift the radial distribution of ε slightly or even convert it from a disklike to a bulge-like galaxy. Below, we present

some examples in which including substructures may shift the radial distribution of ε . Since, by selection, the central galaxy in all of these examples remains MW-like, i.e., demonstrates a well-defined disk, to avoid any confusion about the morphology of the galaxy group, we put a mask over the distance of the particles and disregard stellar particles beyond 150 kpc in computing the total angular momentum and thus in ε . As we show, such a mask removes counterrotating particles, and the final ε distribution remains disklike, i.e., peaks near unity.

Figure 14 presents the radial distribution of ε for a subset of five galaxies representative of our galaxy samples. In every example, the left panel presents the distribution for central particles without any substructures. The middle panel shows ε in the presence of all of the substructures and with no radial truncation. The right panel presents ε with substructures that are truncated above $r = 150$ kpc. From the figure, it manifests that substructures with no radial mask may easily shift the orbital circularity parameter to the left and convert it from a disklike to a bulge-like galaxy.

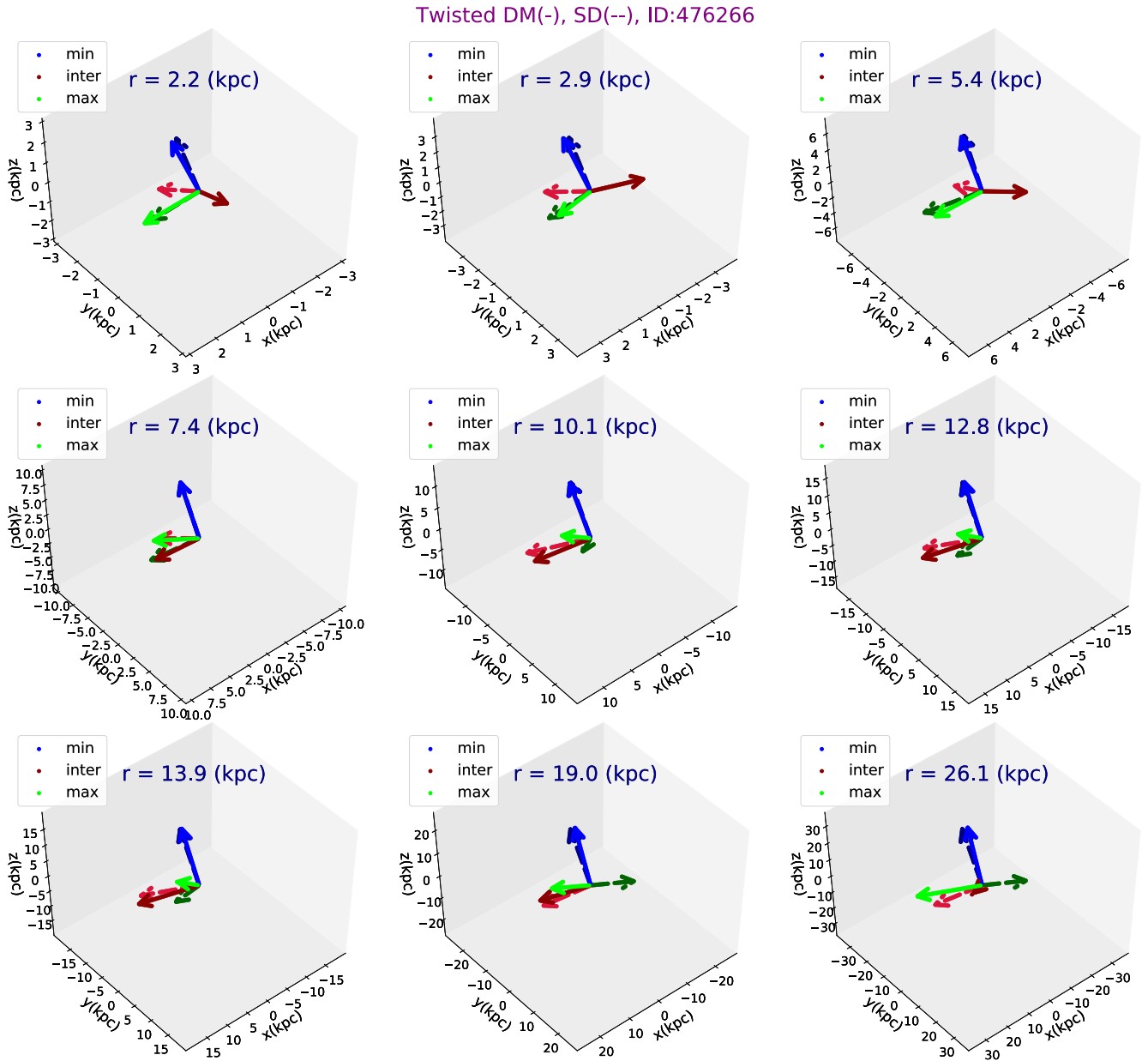


Figure 13. A 3D orientation of the reduced inertia tensor from the DM and SD for one twisted galaxy.

6.2. Impact of FoF Substructures on the Shape

In this section, we investigate the impact of FoF substructures on the shape of the SD, for which we take into account all of the stellar substructures while computing the shape. Figure 15 presents the radial profile of the shape parameters (s , q , T) for the central subhalo and the FoF group halo. It is evidently seen that the profiles of the median and percentiles are fairly close to each other. Furthermore, to get an intuition of what individual galaxies look like, in Figure 16, we draw the Axes/ r ratio for two typical galaxies in the entire sample. Here the left column refers to the central galaxy, while the right column shows the Axes/ r for the FoF group stars. While the profile of the galaxy from the top row shows slightly different behavior, the one from the bottom row is completely similar from the central to FoF group galaxy. The same applies to the rest of the galaxies (not shown), where in some of them, there

are some small changes in the inner part or at the outskirts of the galaxy.

7. Connection to Observations from the Literature

Having computed the shape of SD theoretically, below, we take the first step of comparing this with the observational results from the previous literature. While in our analysis, we remove the impact of the FoF group stars, we skip modeling and removing the stellar streams. Such analysis requires finding reliable models for the stellar streams from the disk and halo, which is beyond the scope of this paper. We defer a comprehensive analysis of the stellar stream to a future work.

As discussed in Bland-Hawthorn & Gerhard (2016, and references therein), measuring the first-order shape and structure of the galaxy is extremely challenging in its own

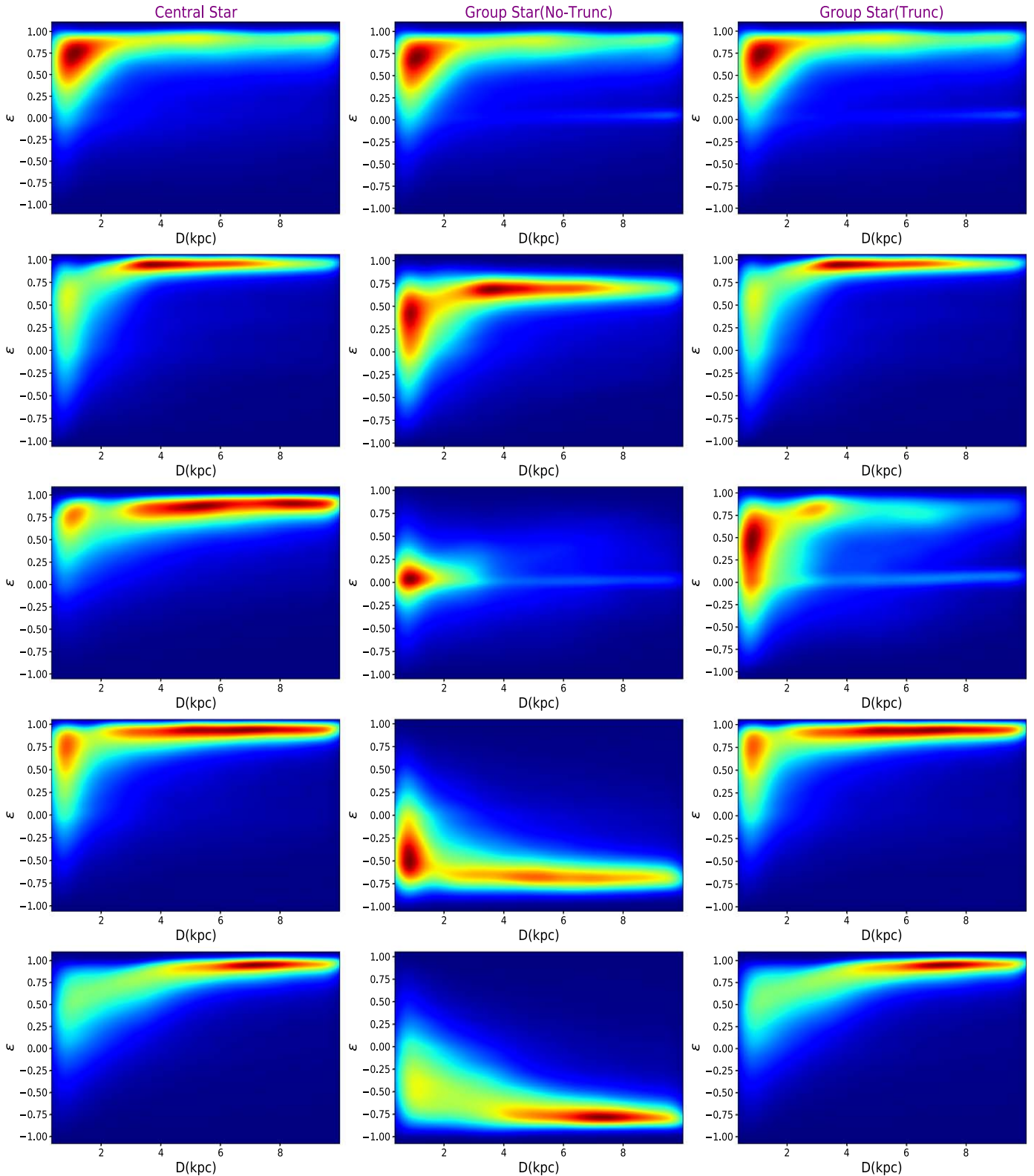


Figure 14. Radial profile of ε for stars in the center (left), the FoF group with no truncation (middle), and FoF stars truncated above 150 kpc (right). Counterrotating farther out substructures may dominantly flip the sign of total angular momentum and thus seem to convert the disk structures. They must therefore be removed when we analyze the radial profile of ε .

right, let alone additional higher-order effects, such as twisting or stretching. As a result, here we instead focus on the shape parameters (s , q) and leave a detailed analysis of twisting and stretching to a future work.

From the observations, we may measure the stellar density profile of the MW halo. There have been several studies trying to estimate the stellar density as a function of radius (Vivas & Zinn 2006; Ivezić et al. 2008; Belokurov et al. 2014).

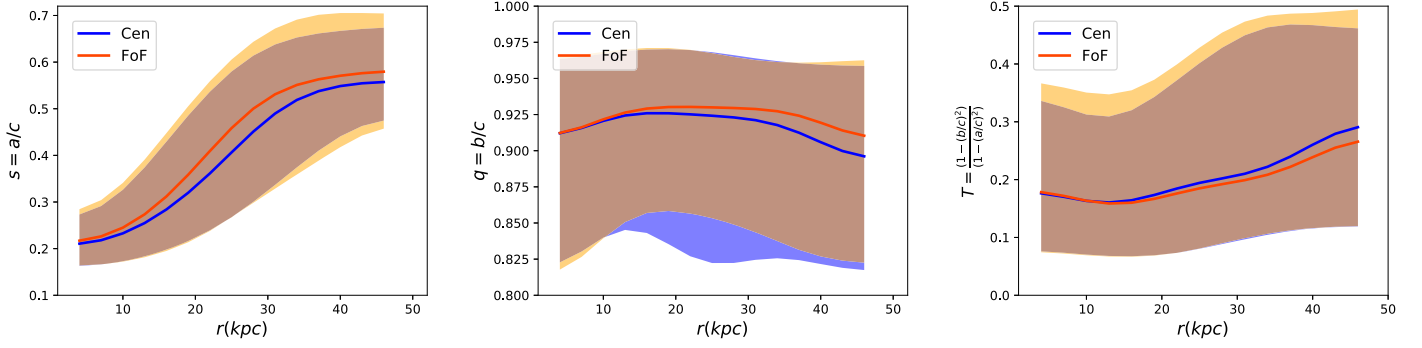


Figure 15. Radial profile of the median and percentile of the shape parameters including the FoF group stars. It is evident that the radial profiles of the median and percentiles of the shape parameters are fairly close between the center (Cen) and substructures (FoF group). This implies that FoF group stars statistically behave the same as the central stars in shaping the SH.

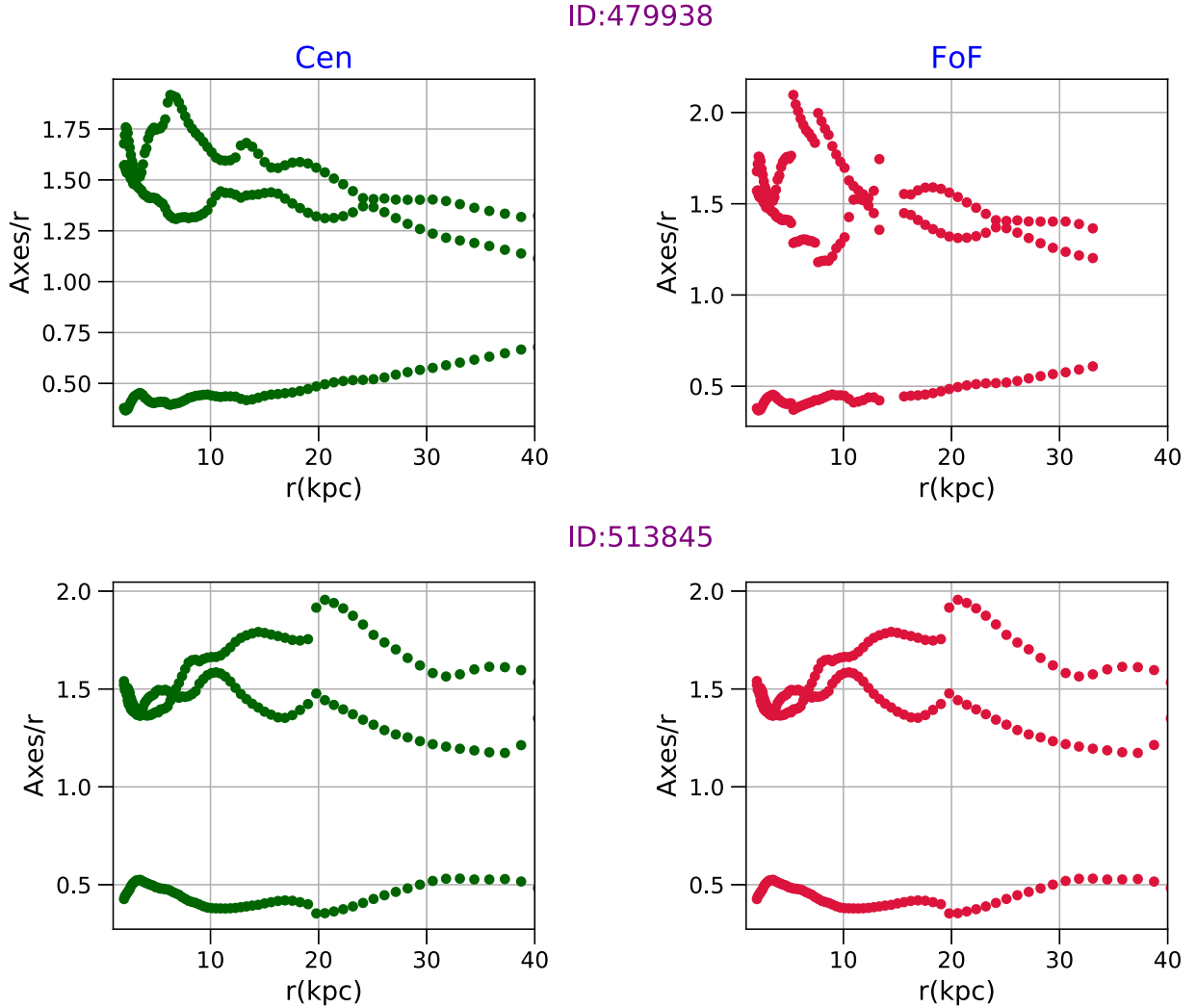


Figure 16. Radial profile of the Axes/ r ratio for two typical galaxies in our sample with (left) and without (right) the substructures. It is seen that FoF group stars do not change the Axes/ r ratio significantly.

Subtracting populations of stars that belong to large substructures (see, e.g., Bell et al. 2008; Belokurov et al. 2014), we end up with a smooth SD component (although more recent work, such as Naidu et al. 2020, has brought even this into question). The inferred density profile can be fitted to various profiles, including a single power law (SPL), a broken power law (BPL), or an Einasto profile. These can also take axisymmetric, $r^2 = (x^2 + y^2 + z^2/q^2)$, or triaxial,

$r^2 = (x^2 + y^2/q^2 + z^2/s^2)$, shapes, with the shape parameters s, q analogous to our shape parameters. Note that since our results point us to a very mild triaxial shape, we expect that comparisons to axisymmetric fits should still remain reasonable.

Using a maximum-likelihood approach, Deason et al. (2011) modeled the density profile of BHB and BS stars and applied it to the photometric catalog of Sloan Digital Sky Survey (SDSS)

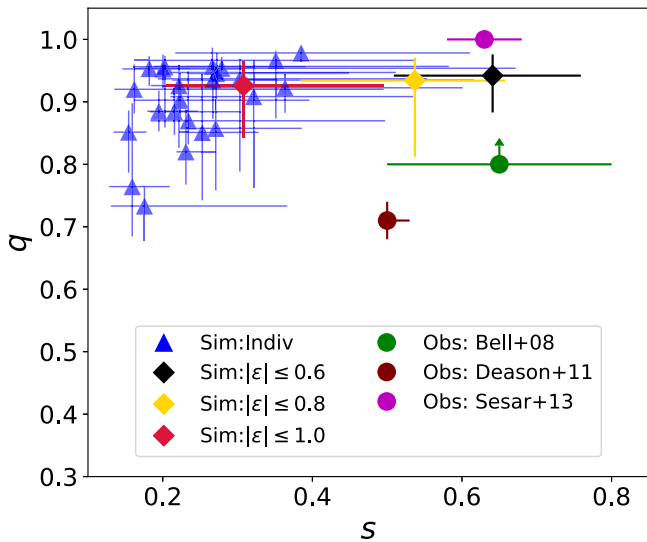


Figure 17. Observational constraints on the shape parameters of SD. Purple, green, and brown circles refer to various observational results, as indicated in the legend. It should be noted that in Sesar et al. (2013), $q = 1$ is an assumption rather than a measurement. Blue triangles denote the median and error bars of (s, q) for individual galaxies in the radial range (4–40) kpc with $\varepsilon \leq 1.0$. The above radial range is chosen to be matched with the observational range of interests (Deason et al. 2011). Red, yellow, and black diamonds display the median and error bars of (s, q) for the full galaxies from our sample in the aforementioned radial range and with $\varepsilon \leq (0.6, 0.8, 1.0)$, respectively. Although we are mainly focused on the SD with $\varepsilon \leq 1.0$, we also show how different ε may contribute in shifting the (s, q) in this plane.

data release 8. As they showed, it provides a robust measurement for the shape of MW SD. As a part of their analysis, they provided the fit to an SPL profile with a triaxial shape and constant shape parameters. Rewriting this in terms of our shape parameters, we get $s = 0.5_{-0.01}^{+0.02}$ and $q = 0.71_{-0.03}^{+0.03}$ covering a radial range of (4–40) kpc. Since this measurement is extended up to 40 kpc, to closely compare our results with that of SDSS, we shall repeat the computation for the median and 16th (84th) percentiles of (s, q) up to this radius. In addition, to fully account for the impact of changing the threshold of ε in the SD, we compute the median (percentiles) of the shape for a few thresholds of ε .

Bell et al. (2008) used a sample of MSTO stars from SDSS DR5 and explored the overall structure of the SD in the MW. They fitted an oblate and triaxial BPL to the data and found a best fit for $0.5 \leq s \leq 0.8$ with a mild triaxial parameter $q \geq 0.8$. Their best fit for s from axisymmetric and triaxial was very similar, indicating that the results of a mild triaxial fit are not very far from the axisymmetric results.

Sesar et al. (2013) used RRLSs chosen from a recalibrated LINEAR data set and fitted an axisymmetric density profile to the data. They found a slightly larger flattening parameter, $s = 0.63 \pm 0.05$, than Deason et al. (2011). This result is compatible with the results of other observational teams using RRLSs (Watkins et al. 2009; Sesar et al. 2010; Faccioli et al. 2014).

Figure 17 summarizes the above constraints on the shape parameters of the SD. Circles with different colors describe different observational results. Blue triangles refer to the median and error bars of (s, q) for individual galaxies in the radial range (4–40) kpc with $\varepsilon \leq 1.0$. The above radial range is chosen to be matched with the observational range of interest (Deason et al. 2011). It is seen that a fraction of galaxies in our

sample may give rise to (s, q) to be fully compatible with the observational results. Red, yellow, and black diamonds display the median and error bars of (s, q) for the full galaxies from our sample in the aforementioned radial range and with $\varepsilon \leq (0.6, 0.8, 1.0)$, respectively. It is intriguing that extending ε shifts the median of s to lower values.

8. Summary and Conclusion

In this paper, we studied the morphology of SDs in a sample of 25 MW-like galaxies in TNG50 of the IllustrisTNG project. We explored the SD shape using two different algorithms. In the first approach, we computed the shape using an EVIM, and in the second (main) approach, we analyzed the shape using an LSIM.

Below, we summarize the main points of the paper.

1. We explicitly showed that while EVIM leads to a smooth shape profile, LSIM gives us more information about the substructures. Owing to this, and as recent observations (Naidu et al. 2020) have shown, the MW is truly made of many substructures, the local-based approach is more favored here, and we have thus used LSIM as the main approach in this work.
2. We inferred the shape at both the statistical and individual levels and classified the galaxies into two different categories. Twisted galaxies present a gradual rotation throughout the galaxy. There are a total of 13 galaxies in this category. Twisted-stretched galaxies, on the other hand, present more abrupt radial rotation. There are 12 galaxies in this class. We visualized the galaxies in both of the above samples and showed that the galaxy is rotating/stretching, respectively.
3. We studied the impact of the threshold on the orbital circularity parameter, ε , in defining the SD in the final inferred shape and explicitly showed that adding more stars from the disk makes the galaxy more oblate.
4. We made a comparison between the DM (Emami et al. 2021) and SH shapes using both EVIM and LSIM, for which we computed the 3×3 matrix of angles between the min, inter, and max eigenvectors in these two methods. The smaller the min–min, inter–inter, and max–max angles are, closer the shape of the DM and SH will be.
5. Quite remarkably, based on the EVIM, closer to the center, the angle profiles between the DM and SH are fairly small, demonstrating that these two profiles are responding to the baryonic gravitational potential from the stellar disk. However, in some cases, these profiles deviate from each other farther out from the center.
6. The inferred angle profile from LSIM, on the other hand, suggests a more oscillating profile. This makes sense, as the inferred eigenvalues from LSIM are closer, in response to the local variations. Therefore, their corresponding eigenvectors reorient more rapidly, owing to the orthogonality at different locations. However, in most cases, it is explicitly seen that while different eigenvalues swing around each other, say, inter and max eigenvalues, the angle between inter–inter and inter–max enhances, but that between inter–max and max–inter decreases. This may imply that the galaxies are close, but it was rather hard to exactly track the inter and max eigenvectors very close to the swing location.

7. We incorporated the impact of the substructures in the orbital circularity parameter and the shape of the SD. In the former case, we explicitly showed that in some cases the substructures located farther out from the center might counterrotate with respect to the stars close by and thus including them with no cutoff, may change the distribution of ε . Owing to this, it is customary to make a radial cutoff, 150 kpc, and eliminate stars that are farther out from the center while computing ε . Computing the shape profile using the filtered set of the aforementioned spatial cut, we showed that the shapes of FoF group stars are fairly similar to the central stars.
8. Finally, we overlaid our theoretical predictions for the shape parameters on top of the data from the previous literature. While the shape measurements from our simulations and the observations are not very different, overall, there are differences in detail that might be due to the fact that different observations have taken different tracers and approaches. It is therefore intriguing to make some mock data and make the comparisons with the data more explicitly. This is, however, left to future work.

We warmly acknowledge the very insightful conversations with Sirio Belli, Charlie Conroy, Daniel Eisenstein, Rohan Naidu, Dylan Nelson, Sandro Tacchella, and Annalisa Pillepich. We also acknowledge the referee for the constructive comments that improved the quality and presentation of this manuscript. R.E. is thankful for support by the Institute for Theory and Computation (ITC) at the Center for Astrophysics (CFA). We are also thankful for the supercomputer facilities at Harvard University, where most of the simulation work was done. M.V. acknowledges support through an MIT RSC award, a Kavli Research Investment Fund, NASA ATP grant NNX17AG29G, and NSF grants AST-1814053, AST-1814259, and AST-1909831. S.B. is supported by Harvard University through the ITC Fellowship. F.M. acknowledges support through the Program ‘‘Rita Levi Montalcini’’ of the Italian MIUR. The TNG50 simulation was realized with computer time granted by the Gauss Centre for Supercomputing (GCS) under the GCS Large-Scale Projects GCS-DWAR on the GCS share of the supercomputer Hazel Hen at HLRS.

Software: h5py (de Buyl et al. 2016), matplotlib (Hunter 2007), numpy (Van der Walt et al. 2011), pandas (McKinney et al. 2010), seaborn (Waskom et al. 2020), scipy (Oliphant 2007).

Data Availability

The data that are directly related to this publication and its figures are available on reasonable request from the corresponding author. The IllustrisTNG simulations themselves are publicly available at www.tng-project.org/data (Nelson et al. 2019). The TNG50 simulation will be made public in the future as well.

Appendix A Shape-finder Algorithms

As already specified in the main text, we have taken the LSIM as the main method. It is, however, intriguing to compute

the shape using a slightly different method and compare the final results to LSIM. Below, we introduce the EVIM method and also make a fair comparison of the shape from different versions of the LSIM and EVIM.

A.1. Enclosed Volume Iterative Method

Generally speaking, EVIM is very similar to LSIM, with the main difference being that at every radius, we replace the thin shell with an enclosed ellipsoid. More specifically, we take the elliptical radius in Equation (5) to be less than unity, meaning that at every radius, in EVIM we compute the shape using all of stars interior to that radii. This may lead to some biases as the number of stars drops significantly from the inner part of the halo to its outer part. Therefore, we get an averaged shape, in which the detailed information about the SD would be lost at larger radii. Indeed, the shape seems to be simple in most cases, with little changes in the radial profile of different angles. This indicates that the average method for stars does not give us a very accurate shape. Owing to this, we skip showing the full details of the results with this approach and instead just present this as a complementary approach.

Figure 3 compares the median and percentiles of the shape parameters inferred using LSIM and EVIM. It is evident that EVIM underestimates the s shape compared with LSIM.

Appendix B Galaxy Classification

As already specified in the main text, we may place the SD shapes in two main categories: twisted galaxies and twisted-stretched galaxies. While we present very few cases in the text, to make the picture clearer, here we present the radial profile of the Axes/ r ratio, the angle of the min-inter-max eigenvectors with a few fixed vectors, and the radial profile of the shape parameters (s , q) for the 25 galaxies in our sample. Also, to have an unambiguous association of angles at initial points, we demand that all of the angles are initially less than 90° .

B.1. Twisted Galaxies

First, we present the population of twisted galaxies. There are a total of 13 twisted galaxies in our sample. Figures 18 and 19 present this class of galaxies. We have truncated the radial profile up to where there is some collection of points for which the shape-finder algorithm does not converge. For example, while the presented galaxies in Figure 18 are converged around (above) 50 kpc, galaxies associated with Figure 19 are mostly converged until 30 kpc continuously and have gaps in between for larger radii. Owing to this, we truncate their shape profile at around 25–30 kpc.

B.2. Twisted-stretched Galaxies

Next, we display the twisted-stretched galaxies, as defined in the main text. There are a total of 12 galaxies in this class. Figures 20 and 21 present the galaxies in this class. In a manner similar to the twisted galaxies, here we truncate the radial profile until we see some gaps in the collection of the converged points.

Twisted Galaxies(1)

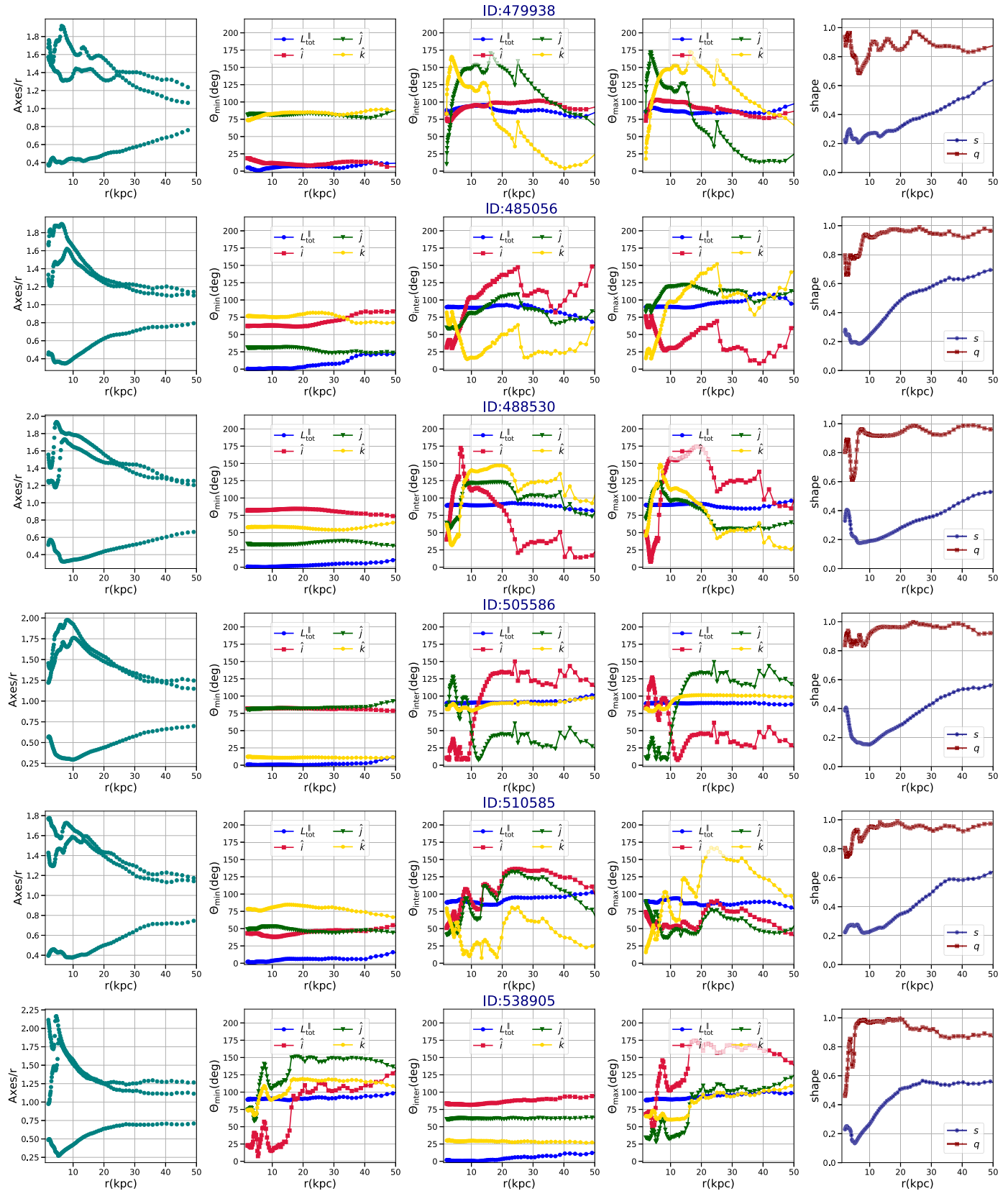


Figure 18. Radial profile of Axes/ r , angles, and shape parameters for the twisted galaxies.

Twisted Galaxies(2)

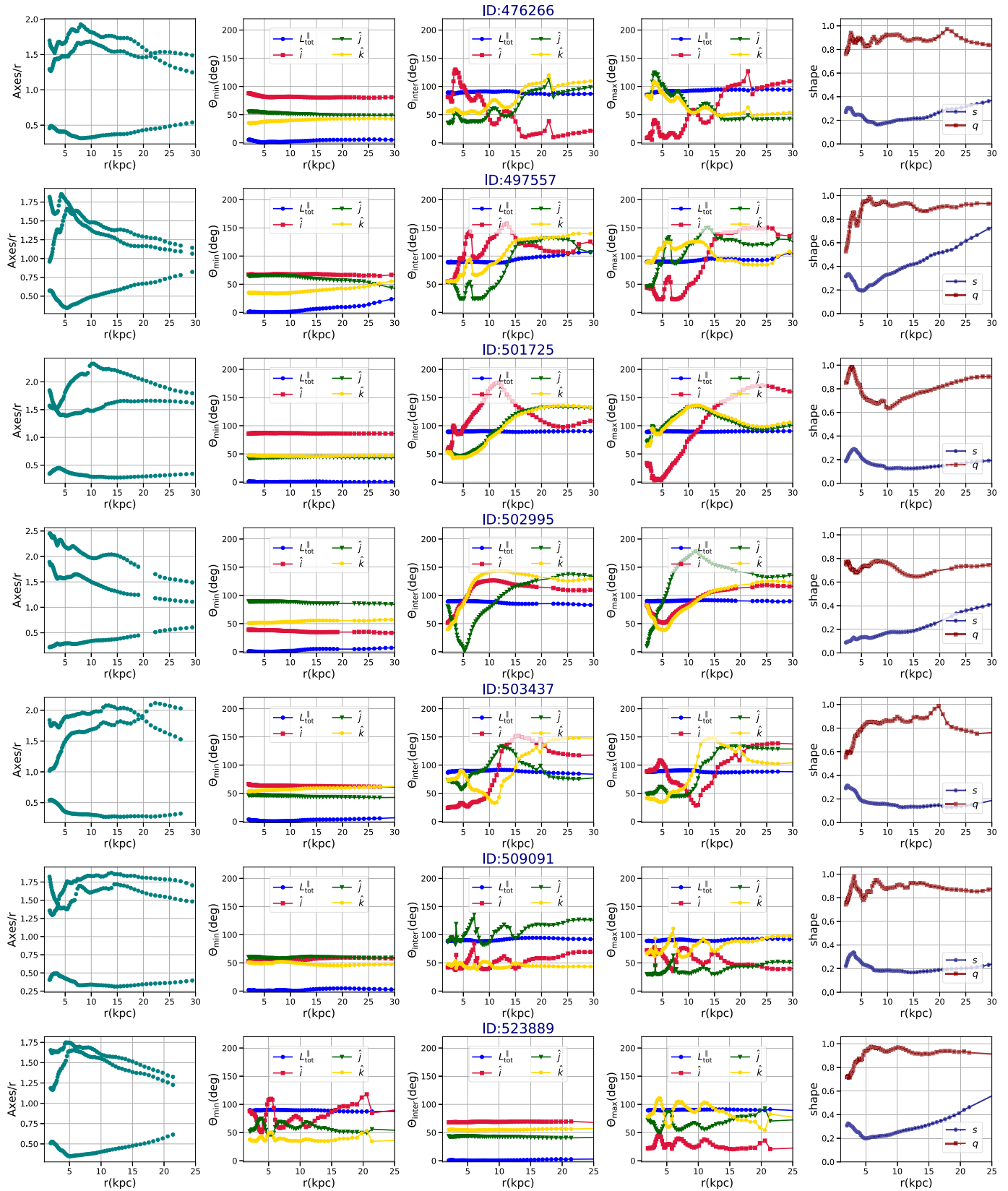


Figure 19. Radial profile of Axes/ r , angles, and shape parameters for the twisted galaxies.

Twisted-Stretched Galaxies(1)

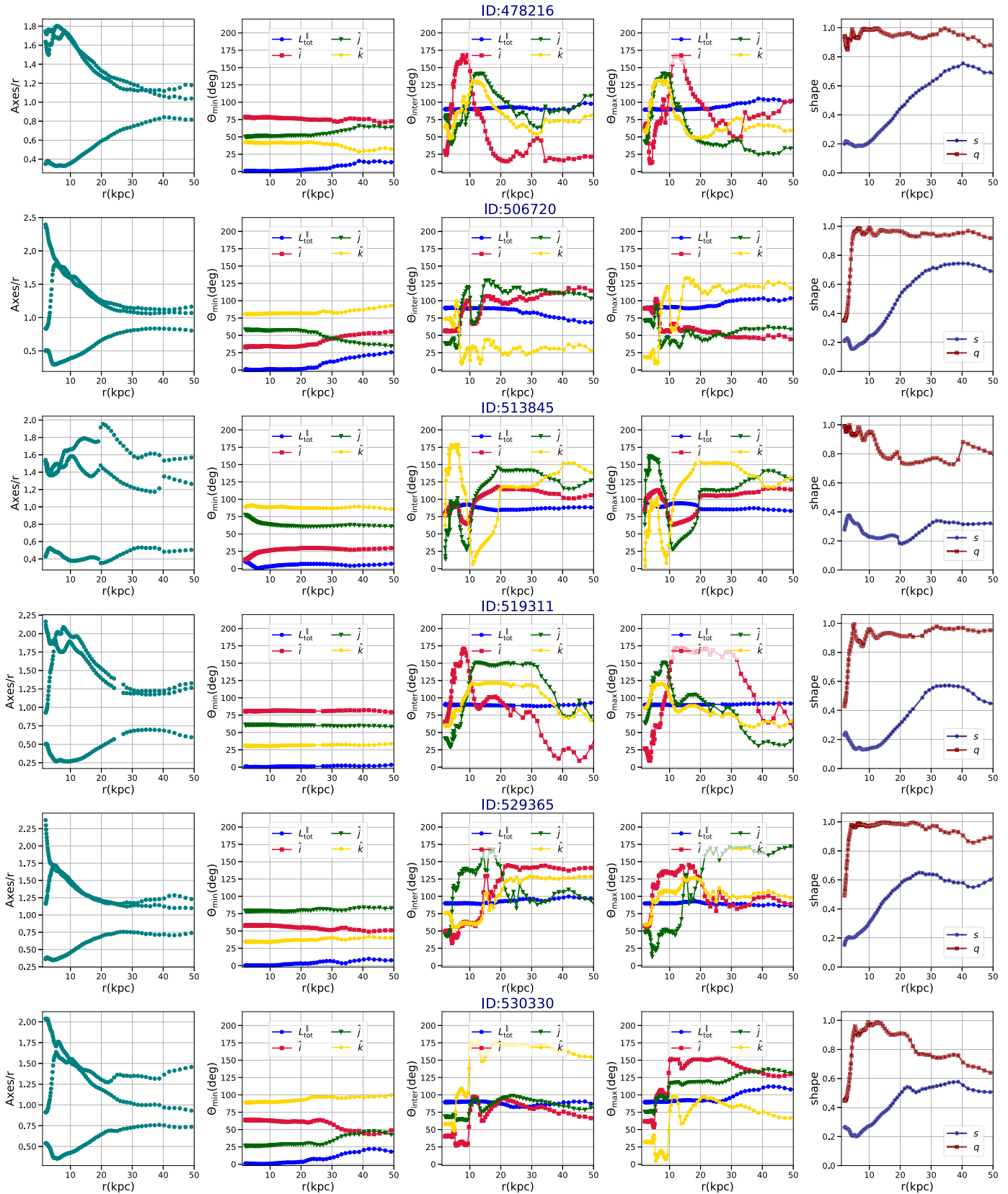


Figure 20. Radial profile of Axes/ r , angles, and shape parameters for the twisted-stretched galaxies.

Twisted-Stretched Galaxies(2)

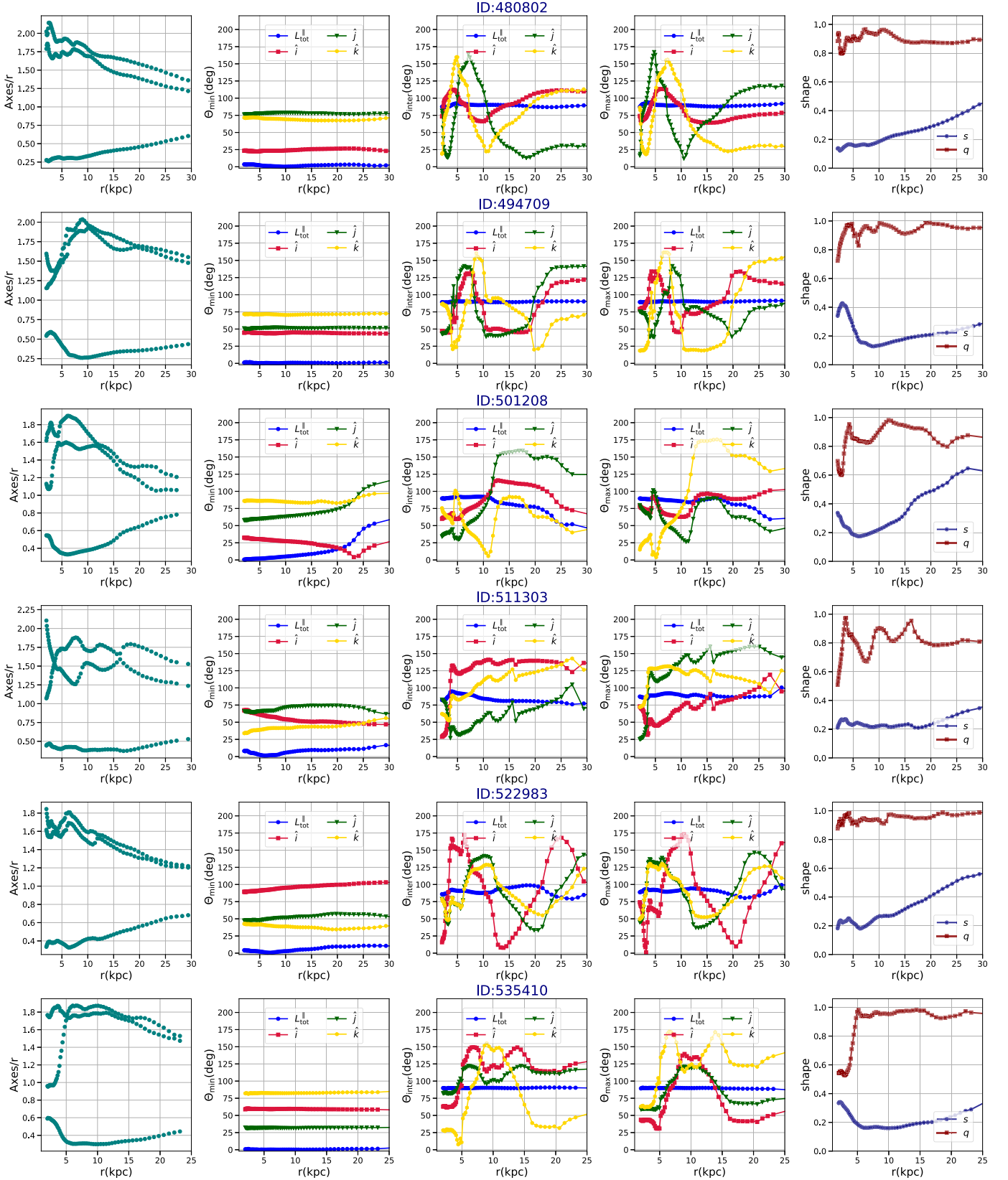




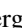
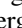

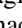



Figure 21. Radial profile of Axes/ r , angles, and shape parameters for the twisted-stretched galaxies.

It is essential to notice that in some cases, such as the galaxies with IDs 506720 and 529365, the galaxy remains completely oblate, $q \simeq 1$, toward large radii. This is associated with a full degeneracy between the intermediate and maximum eigenvalues, a circle in the plane of inter-max eigenvalues. Such symmetry makes it extremely hard to track the radial profile of the angle of the inter and max. In addition, owing to the orthogonality of different eigenvectors, the inferred amount of rotation for these galaxies might be crud. Since in most cases, the galaxy remains almost oblate up to very large distances, almost the edge of the SD, we may not focus on the outer radii to make the classification. Owing to this, we put such galaxies in the twisted-stretched class. It would be intriguing to track the galaxy morphology with the redshift and see how the radial profile of the angles changes. This is, however, beyond the scope of the current work and left to a future study.

ORCID iDs

Razieh Emami  <https://orcid.org/0000-0002-2791-5011>
 Lars Hernquist  <https://orcid.org/0000-0001-6950-1629>
 Shy Genel  <https://orcid.org/0000-0002-3185-1540>
 Sownak Bose  <https://orcid.org/0000-0002-0974-5266>
 Rainer Weinberger  <https://orcid.org/0000-0001-6260-9709>
 Mark Vogelsberger  <https://orcid.org/0000-0001-8593-7692>
 Joshua S. Speagle  <https://orcid.org/0000-0003-2573-9832>
 Federico Marinacci  <https://orcid.org/0000-0003-3816-7028>
 Paul Torrey  <https://orcid.org/0000-0002-5653-0786>

References

- Abadi, M. G., Navarro, J. F., Steinmetz, M., et al. 2003, *ApJ*, 591, 499
 Bailin, J., Kawata, D., Gibson, B. K., et al. 2005, *ApJL*, 627, L17
 Beasley, M. A., Trujillo, I., Leaman, R., et al. 2018, *Natur*, 555, 483
 Bell, E. F., Zucker, D. B., Belokurov, V., et al. 2008, *ApJ*, 680, 295
 Belokurov, V., Koposov, S. E., Evans, N. W., et al. 2014, *MNRAS*, 437, 116
 Bird, S. A., Xue, X.-X., Liu, C., et al. 2020, arXiv:2005.05980
 Bland-Hawthorn, J., & Gerhard, O. 2016, *ARA&A*, 54, 529
 Blumenthal, G. R., Faber, S. M., Primack, J. R., & Rees, M. J. 1984, *Natur*, 311, 517
 Buck, T., Macciò, A., Ness, M., et al. 2018, in Proc. IAU Symp. 334, Rediscovering our Galaxy (Cambridge: Cambridge Univ. Press), 209
 Buck, T., Obreja, A., Macciò, A. V., et al. 2020, *MNRAS*, 491, 3461
 Crain, R. A., Schaye, J., Bower, R. G., et al. 2015, *MNRAS*, 450, 1937
 de Buyl, P., Huang, M.-J., & Deprez, L. 2016, arXiv:1608.04904
 Deason, A. J., Belokurov, V., & Evans, N. W. 2011, *MNRAS*, 416, 2903
 El-Badry, K., Quataert, E., Wetzel, A., et al. 2018, *MNRAS*, 473, 1930
 Emami, R., Genel, S., Hernquist, L., et al. 2021, *ApJ*, 913, 36
 Faccioli, L., Smith, M. C., Yuan, H.-B., et al. 2014, *ApJ*, 788, 105
 Font, A. S., McCarthy, I. G., Poole-Mckenzie, R., et al. 2020, *MNRAS*, 498, 1765
 Forbes, D. A., Brodie, J. P., & Grillmair, C. J. 1997, *AJ*, 113, 1652
 Garrison-Kimmel, S., Hopkins, P. F., Wetzel, A., et al. 2018, *MNRAS*, 481, 4133
 Genel, S., Vogelsberger, M., Springel, V., et al. 2014, *MNRAS*, 445, 175
 Grand, R. J. J., Helly, J., Fattahi, A., et al. 2018, *MNRAS*, 481, 1726
 Hani, M. H., Ellison, S. L., Sparre, M., et al. 2019, *MNRAS*, 488, 135
 Helmi, A., Babusiaux, C., Koppelman, H. H., et al. 2018, *Natur*, 563, 85
 Helmi, A., & White, S. D. M. 1999, *MNRAS*, 307, 495
 Hunter, J. D. 2007, *CSE*, 9, 90
 Ibata, R. A., Gilmore, G., & Irwin, M. J. 1994, *Natur*, 370, 194
 Iorio, G., & Belokurov, V. 2019, *MNRAS*, 482, 3868
 Iorio, G., & Belokurov, V. 2021, *MNRAS*, 502, 5686
 Ivezić, Ž., Sesar, B., Jurić, M., et al. 2008, *ApJ*, 684, 287
 Kado-Fong, E., Greene, J. E., Huang, S., et al. 2020, *ApJ*, 900, 163
 Mackereth, J. T., & Bovy, J. 2020, *MNRAS*, 492, 3631
 Marinacci, F., Vogelsberger, M., Pakmor, R., et al. 2018, *MNRAS*, 480, 5113
 McKinney, W., et al. 2010, in Proc. IX Python in Science Conf. 445 (Austin, TX: SciPy), 51
 Merritt, A., Pillepich, A., van Dokkum, P., et al. 2020, *MNRAS*, 495, 4570
 Monachesi, A., Gómez, F. A., Grand, R. J. J., et al. 2016, *MNRAS*, 459, L46
 Monachesi, A., Gómez, F. A., Grand, R. J. J., et al. 2019, *MNRAS*, 485, 2589
 Myeong, G. C., Vasiliev, E., Iorio, G., et al. 2019, *MNRAS*, 488, 1235
 Naidu, R. P., Conroy, C., Bonaca, A., et al. 2020, *ApJ*, 901, 48
 Naiman, J. P., Pillepich, A., Springel, V., et al. 2018, *MNRAS*, 477, 1206
 Navarro, J. F., Frenk, C. S., & White, S. D. M. 1997, *ApJ*, 490, 493
 Nelson, D., Pillepich, A., Springel, V., et al. 2018, *MNRAS*, 475, 624
 Nelson, D., Pillepich, A., Springel, V., et al. 2019, *MNRAS*, 490, 3234
 Nelson, D., Springel, V., Pillepich, A., et al. 2019, *ComAC*, 6, 2
 Oliphant, T. E. 2007, *CSE*, 9, 10
 Orr, M. E., Hayward, C. C., Medling, A. M., et al. 2020, *MNRAS*, 496, 1620
 Oser, L., Ostriker, J. P., Naab, T., et al. 2010, *ApJ*, 725, 2312
 Pillepich, A., Nelson, D., Hernquist, L., et al. 2018, *MNRAS*, 475, 648
 Pillepich, A., Nelson, D., Springel, V., et al. 2019, *MNRAS*, 490, 3196
 Pillepich, A., Springel, V., Nelson, D., et al. 2018, *MNRAS*, 473, 4077
 Planck Collaboration, Ade, P. A. R., Aghanim, N., et al. 2016, *A&A*, 594, A13
 Posti, L., & Helmi, A. 2019, *A&A*, 621, A56
 Prada, J., Forero-Romero, J. E., Grand, R. J. J., et al. 2019, *MNRAS*, 490, 4877
 Sanderson, R. E., Wetzel, A., Loebman, S., et al. 2020, *ApJS*, 246, 6
 Santistevan, I. B., Wetzel, A., El-Badry, K., et al. 2020, *MNRAS*, 497, 747
 Schaye, J., Crain, R. A., Bower, R. G., et al. 2015, *MNRAS*, 446, 521
 Schinnerer, E., Meidt, S. E., Pety, J., et al. 2013, *ApJ*, 779, 42
 Schulze, F., Remus, R.-S., Dolag, K., et al. 2020, *MNRAS*, 493, 3778
 Searle, L., & Zinn, R. 1978, *ApJ*, 225, 357
 Sesar, B., Ivezić, Ž., Grammer, S. H., et al. 2010, *ApJ*, 708, 717
 Sesar, B., Ivezić, Ž., Stuart, J. S., et al. 2013, *AJ*, 146, 21
 Shao, S., Cautun, M., Frenk, C. S., et al. 2016, *MNRAS*, 460, 3772
 Sijacki, D., Vogelsberger, M., Genel, S., et al. 2015, *MNRAS*, 452, 575
 Springel, V. 2010, *MNRAS*, 401, 791
 Springel, V., Pakmor, R., Pillepich, A., et al. 2018, *MNRAS*, 475, 676
 Tenny, A., Mandelbaum, R., Di Matteo, T., et al. 2014, *MNRAS*, 441, 470
 Trayford, J. W., Frenk, C. S., Theuns, T., et al. 2019, *MNRAS*, 483, 744
 Van der Walt, S., Colbert, S. C., & Varoquaux, G. 2011, *CSE*, 13, 22
 Vivas, A. K., & Zinn, R. 2006, *AJ*, 132, 714
 Vogelsberger, M., Genel, S., Springel, V., et al. 2014a, *MNRAS*, 444, 1518
 Vogelsberger, M., Genel, S., Springel, V., et al. 2014b, *Natur*, 509, 177
 Vogelsberger, M., Marinacci, F., Torrey, P., et al. 2020, *NatRP*, 2, 42
 Waskom, M., Botvinnik, O., Ostblom, J., et al. 2020, mwaskom/seaborn: v0.10.0 (2020 January), v0.10.0. Zenodo, doi:10.5281/zenodo.3629446
 Watkins, L. L., Evans, N. W., Belokurov, V., et al. 2009, *MNRAS*, 398, 1757
 Weinberger, R., Springel, V., Hernquist, L., et al. 2017, *MNRAS*, 465, 3291
 White, S. D. M., & Frenk, C. S. 1991, *ApJ*, 379, 52
 White, S. D. M., & Rees, M. J. 1978, *MNRAS*, 183, 341
 Zemp, M., Gnedin, O. Y., Gnedin, N. Y., et al. 2011, *ApJS*, 197, 30